Article

Current Biology

Actin Turnover in Lamellipodial Fragments

Graphical Abstract

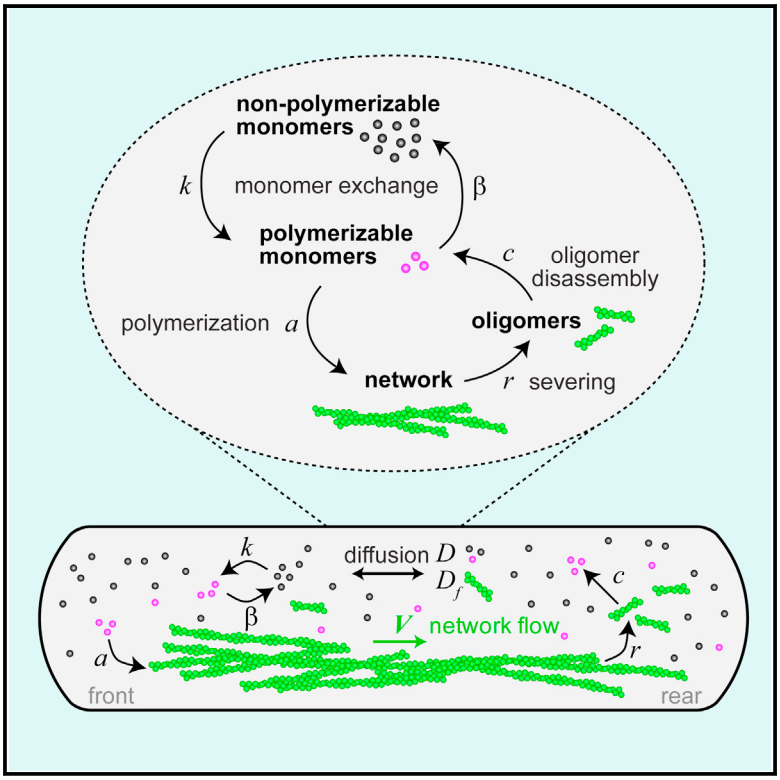

Authors

Dikla Raz-Ben Aroush, Noa Ofer, Enas Abu-Shah, Jun Allard, Oleg Krichevsky, Alex Mogilner, Kinneret Keren

Correspondence

mogilner@cims.nyu.edu (A.M.), kinneret@physics.technion.ac.il (K.K.)

In Brief

Raz-Ben Aroush et al. combine experimental measurements with mathematical modeling to quantitatively characterize actin turnover in lamellipodial fragments. Although the network assembles and disassembles locally, most of the actin subunits diffuse as monomers or short oligomers, moving across the entire lamellipodium before reassembling into the network.

Highlights

- The actin network turns over locally throughout the lamellipodium
- A large fraction of the diffusible actin pool is in the form of short oligomers
- The majority of actin monomers are transiently kept in a non-polymerizable pool
- Actin subunits typically diffuse across the entire lamellipodium before reassembling

Raz-Ben Aroush et al., 2017, Current Biology *27*, 2963–2973
October 9, 2017
http://dx.doi.org/10.1016/j.cub.2017.08.066

Current Biology
Article

Actin Turnover in Lamellipodial Fragments

Dikla Raz-Ben Aroush,[1,7] Noa Ofer,[1,2,7] Enas Abu-Shah,[1,2,8] Jun Allard,[3] Oleg Krichevsky,[4] Alex Mogilner,[5,*] and Kinneret Keren[1,2,6,9,*]

[1]Department of Physics, Technion–Israel Institute of Technology, Haifa 32000, Israel
[2]Russell Berrie Nanotechnology Institute, Technion–Israel Institute of Technology, Haifa 32000, Israel
[3]Department of Mathematics, Center for Complex Biological Systems and Department of Physics and Astronomy, University of California at Irvine, Irvine, CA 92697, USA
[4]Physics Department and Ilse Kats Center for Nanoscience, Ben-Gurion University, Beer-Sheva 84105, Israel
[5]Courant Institute of Mathematical Sciences and Department of Biology, New York University, New York, NY 10012, USA
[6]Network Biology Research Laboratories, Technion–Israel Institute of Technology, Haifa 32000, Israel
[7]These authors contributed equally
[8]Present address: Kennedy Institute of Rheumatology, University of Oxford, Oxford OX3 7FY, UK
[9]Lead Contact
*Correspondence: mogilner@cims.nyu.edu (A.M.), kinneret@physics.technion.ac.il (K.K.)
http://dx.doi.org/10.1016/j.cub.2017.08.066

SUMMARY

Actin turnover is the central driving force underlying lamellipodial motility. The molecular components involved are largely known, and their properties have been studied extensively in vitro. However, a comprehensive picture of actin turnover in vivo is still missing. We focus on fragments from fish epithelial keratocytes, which are essentially stand-alone motile lamellipodia. The geometric simplicity of the fragments and the absence of additional actin structures allow us to characterize the spatiotemporal lamellipodial actin organization with unprecedented detail. We use fluorescence recovery after photobleaching, fluorescence correlation spectroscopy, and extraction experiments to show that about two-thirds of the lamellipodial actin diffuses in the cytoplasm with nearly uniform density, whereas the rest forms the treadmilling polymer network. Roughly a quarter of the diffusible actin pool is in filamentous form as diffusing oligomers, indicating that severing and debranching are important steps in the disassembly process generating oligomers as intermediates. The remaining diffusible actin concentration is orders of magnitude higher than the in vitro actin monomer concentration required to support the observed polymerization rates, implying that the majority of monomers are transiently kept in a non-polymerizable "reserve" pool. The actin network disassembles and reassembles throughout the lamellipodium within seconds, so the lamellipodial network turnover is *local*. The diffusible actin transport, on the other hand, is *global*: actin subunits typically diffuse across the entire lamellipodium before reassembling into the network. This combination of local network turnover and global transport of dissociated subunits through the cytoplasm makes actin transport robust yet rapidly adaptable and amenable to regulation.

INTRODUCTION

Cell motility is fundamentally important in morphogenesis, wound healing, and the immune response. One of the best-studied basic types of cell movement is lamellipodial motility [1, 2], characterized by a thin (~0.1–0.2 μm), broad (~10–40 μm) motile appendage containing a dynamic actin network enveloped by the plasma membrane [3]. Lamellipodial protrusion is driven by actin polymerization at the leading edge [4] (Figure S1A). As new actin assembles at the front, older filaments are pushed away from the leading edge and eventually disassemble. Despite substantial progress in studying the regulation of lamellipodial actin dynamics [2, 5, 6], its complexity still defies quantitative understanding [7].

Here we focus on actin turnover, which is a fundamental part of lamellipodial motility. Two possible limiting scenarios for actin turnover have been put forward: the network-treadmilling model [8–10], in which actin assembly occurs primarily at the leading edge with slow network disassembly everywhere (global network turnover; Figure S1Bii), and the nucleation-release model [11, 12], where rapid actin assembly and disassembly take place throughout the lamellipodium (local network turnover; Figure S1Biii). Measurements of the actin turnover rates in the lamellipodium support the nucleation-release model in some cell types [12–15] and network treadmilling in other cell types [16] (see STAR Methods).

Actin turnover and recycling in vivo involve a host of actin-binding proteins that associate with actin monomers and/or filaments. The different actin subpopulations interchange continuously, and this has a substantial effect on the dynamics, as each subpopulation is characterized by different kinetics [2, 4]. The relative size of the actin subpopulations is largely unknown, as direct measurements by techniques such as labeling with actin-binding probes, photoactivation, or cell extraction cannot discriminate between all the various subpopulations [4, 17–21]. It is also unclear how the presence of monomer-binding proteins including thymosin and profilin influence the effective critical concentration of actin in vivo (see STAR Methods). To add to this complexity, recent research shows that the synergistic action of several proteins, including coronin, cofilin, Aip1, twinfilin,

and Srv2/CAP [22–25], as well as the activity of myosin motors [26, 27] accelerate network disassembly by promoting filament severing and debranching, which leads to the production of actin oligomers. Importantly, these studies imply that the actin network does not disassemble into monomers directly but rather first breaks into short actin filaments, which are disconnected from the network and small enough to diffuse in the cytoplasm.

Because a detailed molecular picture of all the reactions involved in actin turnover in motile cells is still beyond reach [6, 28], our aim here is to characterize actin turnover and transport in a coarse-grained yet quantitative manner. We seek to measure the spatial distributions of the main lamellipodial actin subpopulations and the transitions between them. To avoid complications related to fluctuating actin concentrations, heterogeneous lamellipodium-lamellum actin networks [29], or the presence of a cell body with a cortical actin network that obscures measurements in the rear part of the cell, we use lamellipodial fragments from motile keratocytes [30, 31]. These fragments have a simple, persistent geometry and undergo rapid movement like whole cells, while lacking a cell body and any competing actin structures. Using this model system, we characterize the steady-state lamellipodial dynamics with unprecedented detail, combining experimental measurements with mathematical analysis to generate a comprehensive picture of actin turnover. We find that there is roughly 2-fold more actin in the diffusible pool compared to the network, and show that oligomers constitute a sizable fraction of this diffusible pool. The network turns over rapidly and locally, with actin assembly and disassembly occurring within seconds throughout the lamellipodium, while the diffusible actin remains nearly uniformly distributed. The model suggests that even though the actin network turnover is local, monomer transport is global. This global transport is made possible by the vast amount of non-polymerizable actin, which exchanges rapidly with the polymerizable actin pool. Consequently, actin subunits typically diffuse across the lamellipodium before reassembling into the network. This has profound implications for lamellipodial motility, allowing cells to move in a robust manner yet maintain the ability to rapidly adapt to changing conditions.

RESULTS

The Majority of Actin Is Diffusible

To measure the filamentous actin density in fragments in absolute numbers, exogenous actin filaments are added as standard markers and the fragments and filaments are fixed and stained with phalloidin [3]. The filamentous actin density in the lamellipodium is determined by quantitative densitometry, using the added filaments to calibrate the fluorescence intensity per filament (Figures 1A–1C; STAR Methods). We find that the average actin filament area density in the lamellipodium is 400 ± 100 (μm filaments)/μm^2 (mean ± SD). Assuming that the lamellipodial thickness is ~200 nm [3, 32], this translates to an average molar concentration of 1,200 ± 300 μM actin subunits in filamentous form (Figure 1C). These values are comparable to lamellipodial actin filament concentrations in other cell types, measured by this method [3] or by counting filaments in electron micrographs [17, 33] (e.g., 1,600 μM in fibroblasts [3], 500 μM in B16-F1 cells [17]). The filament density goes down as a function of distance from the leading edge (Figures 1A and 1B), indicating that there is net disassembly throughout the lamellipodium. Near the trailing edge, this trend reverses, and the density increases as filamentous actin accumulates at the rear boundary.

A large fraction of the actin in the lamellipodium is not associated with the network. To obtain quantitative information regarding the size of this diffusible actin pool, we compare the amount of actin before and after extracting the diffusible cytosolic constituents (Figure 1D) [17]. We introduce low levels of fluorescent actin (<1% of endogenous actin levels) into lamellipodial fragments by electroporation, and use Triton X-100 to rapidly disrupt the membrane in the presence of high-molecular-weight polyethylene glycol (PEG) and phalloidin, which stabilize the network. This extraction protocol has been shown to preserve the filamentous actin network [17, 34] while effectively removing soluble components (Figure 1D). Thus, the fluorescence signal before extraction reflects the cumulative distribution of all actin subpopulations (Figures 1D and 1E), whereas the actin signal after extraction is only due to the non-diffusible network actin (Figures 1D and 1F). The amount of diffusible actin is determined from the difference in the fluorescence intensity before and after extraction for each fragment. We find that on average ~70% of the actin in fragments resides in the diffusible actin pool, whereas the remaining ~30% forms the filamentous lamellipodial network (Figure 1G).

Uncapped Barbed and Pointed Ends Are Distributed throughout the Lamellipodium

The turnover dynamics of actin filaments occur preferentially at filament ends, with polymerization occurring at uncapped barbed ends and depolymerization at pointed ends [1, 6]. To map the distribution of uncapped filament ends, we permeabilize fragments, following a brief fixation step, and introduce fluorescent actin monomers that polymerize onto the uncapped filament ends and label them [35, 36]. Two different types of labeled actin are used to label the barbed and pointed ends distinctly [36]. This is combined with phalloidin labeling to obtain a tertiary stain of the filamentous actin and the uncapped barbed and pointed ends, all within the same fragment (Figure 2).

We find that uncapped barbed ends are enriched at the leading edge (Figures 2A and 2D), while the pointed ends are biased toward the rear (Figures 2A and 2E). A ratio image of the barbed end labeling over the pointed end labeling clearly illustrates the spatial polarization of the lamellipodial actin network, with barbed end enhancement near the leading edge (Figure 2C). However, the majority of uncapped barbed ends are distributed throughout the lamellipodium: less than 10% of the uncapped barbed ends are localized within 1 μm of the leading edge, while the remaining ~90% are broadly spread throughout the lamellipodium (Figure 2G). Thus, a substantial portion of actin assembly is expected to occur away from the leading edge. Similarly, we find a broad distribution of uncapped pointed ends throughout the lamellipodium (Figure 2E), indicating that disassembly processes are also widespread.

The Lamellipodial Actin Network Turns over Rapidly

The turnover of the lamellipodial network is characterized by following the fluorescence recovery after photobleaching (FRAP) of actin. Two different types of labeled actin probes are

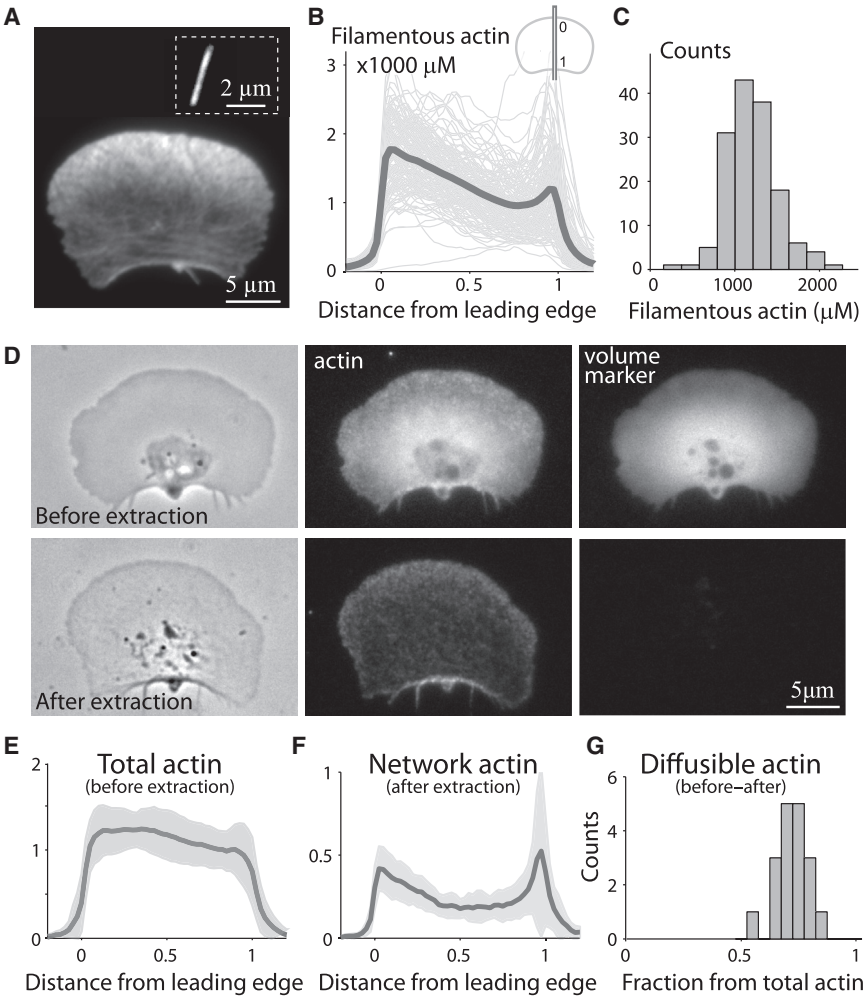

Figure 1. Quantitative Analysis of Actin in Fragments

(A–C) Quantitative measurements of the filamentous actin in fragments.

(A) Fluorescence images of a fragment and a filament (inset) after fixing and staining with Alexa Fluor 546-phalloidin. The exposure times are 100× longer for filaments compared to fragments.

(B) The molar filamentous actin concentration (subunits per volume) as determined by quantifying the number of actin filaments per unit area and assuming a uniform lamellipodial thickness of 0.2 μm (see STAR Methods). The filamentous actin concentration along a cross-section is shown as a function of the normalized distance from the leading edge (front-to-rear distance = 1). Traces for individual fragments are plotted (thin lines) along with the population average (thick line).

(C) A histogram of the average filamentous actin concentration in individual fragments for the population of fragments shown in (B).

(D–G) Extraction experiments show that most of the lamellipodial actin is diffusible.

(D) Phase-contrast and fluorescence images showing the distribution of Alexa Fluor 488-actin and Texas red 3kDa dextran in the same fragment, before (top) and after extraction (bottom). The diffusible cytoplasmic constituents, including the diffusible actin and the dextran volume marker, are removed during the extraction step.

(E) The distribution of total actin in fragments along a cross-section from front to rear, perpendicular to the leading edge. The population-average actin intensity before extraction (N = 18) (thick line) is plotted together with the SD (shaded region). The actin intensity within each fragment is normalized to have mean 1.

(F) The distribution of non-diffusible (network) actin in fragments along a cross-section from front to rear. The population-average actin intensity after extraction (N = 18) (thick line) is plotted together with the SD (shaded region). The intensity normalization within each fragment is determined before extraction (as in E) to have mean 1, so the intensities after extraction reflect the relative fraction of the network actin from the total actin.

(G) A histogram of the fraction of diffusible actin in fragments, determined from the difference between the integrated actin signal in fragments before extraction (total actin) and after extraction (network actin). The average diffusible actin fraction is 0.69 ± 0.16 (mean ± SD; N = 18).

introduced into fragments by electroporation (Figure 3A; STAR Methods). An ~1 μm region of interest (ROI) near the center of the leading edge is bleached in one channel, whereas the second channel is used as a reference, to correct for local variations in actin density. The recovery time for the diffusible actin after bleaching (through diffusion of unbleached actin into the ROI) is shorter than the duration of the bleaching step (~0.5 s). Thus, the relative drop in the ROI fluorescence intensity in the first frame after bleaching is a measure of the fraction of non-diffusible network actin (Figure 3C). We find that about a third of the lamellipodial actin is associated with the network, whereas the remaining two-thirds forms the diffusible actin pool (Figure 3E). These results are in excellent agreement with the extraction experiments, which provide an independent measure of the fraction of diffusible actin (Figure 1G).

The network turnover rate can be determined from the recovery of the actin signal after bleaching. To correct for overall actin density variations as the fragment moves forward, we consider the ratio between the signal intensity in the bleached channel and the control channel (Figures 3B and 3C). The lamellipodial network in keratocyte fragments exhibits negligible retrograde flow in the lab frame of reference [31], so the bleached network remains essentially stationary in the lab frame of reference as the fragment moves forward (Figure 3B). We find that the recovery time of the average ratio signal is ~4 s (Figure 3C), and does not vary significantly as a function of distance from the leading edge (Figure S2F). Fitting the ROI ratio signal in each fragment separately and averaging the recovery times determined for individual fragments gives a similar value (Figure 3D). The rapid recovery measured in the FRAP experiments indicates that network assembly processes are not restricted to the leading edge, consistent with the broad distribution of uncapped actin filament ends (Figure 2).

Interestingly, the actin levels in the bleached channel do not return to the level of the reference actin channel even after >15 s. This is reflected in the ROI ratio signal, which recovers to only ~90% of its original value (Figure 3C). These observations suggest that whereas most of the actin filaments turn over

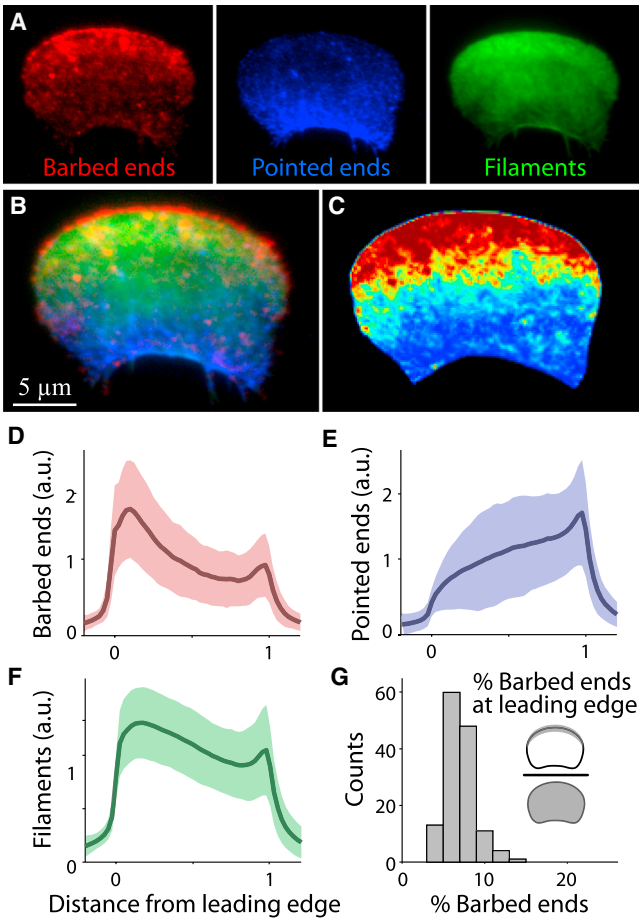

Figure 2. The Distribution of Uncapped Actin Filament Ends

(A) Fluorescence images showing the distributions of uncapped barbed ends (red; rhodamine-actin), uncapped pointed ends (blue; Alexa Fluor 488-actin), and filamentous actin (green; Alexa Fluor 680-phalloidin) in a fragment following fixation and end labeling (STAR Methods).

(B) An overlay of the uncapped barbed ends, uncapped pointed ends, and actin network density for the fragment shown in (A).

(C) A ratio image depicting the barbed end signal divided by the pointed end signal for the fragment shown in (A).

(D–F) The intensity along a cross-section perpendicular to the leading edge is plotted as a function of the normalized distance from the leading edge for uncapped barbed end labeling (D), uncapped pointed end labeling (E), and filamentous actin (F). Population averages (lines; N = 137) are shown together with the SD (shaded regions).

(G) The percentage of uncapped barbed ends at the leading edge is calculated by taking the ratio of the integrated fluorescence intensity of barbed end staining in a 1-μm-wide strip along the leading edge and the integrated signal over the whole fragment. A histogram of the percentage of uncapped barbed ends at the leading edge in a population of fragments is shown.

rapidly, some of the filaments are substantially more stable and remain associated with the network for considerably longer.

The Diffusible Actin Pool Contains a Significant Amount of Oligomers

To characterize the components of the diffusible actin pool, we turn to fluorescence correlation spectroscopy (FCS) experiments, which probe the dynamics of molecules at much shorter timescales (Figures 4A–4C). Distinct actin subpopulations are examined using different probes conjugated to the same fluorophore. Specifically, we use Alexa Fluor 488-actin, which incorporates into all actin subpopulations, Alexa Fluor 488-phalloidin, which associates with filamentous actin, and a free Alexa Fluor 488, which has comparable size to phalloidin but does not bind actin. Each probe is first calibrated in solution and then electroporated at low levels into fragments (STAR Methods). Because the fragments are moving, we perform FCS measurements by positioning a stationary laser beam in front of the motile fragments, so that the beam crosses the lamellipodium along its midline, perpendicular to the leading edge, as the fragments translocate forward (Figure 4A). The fluorescence autocorrelation function is averaged within the lamellipodium over ~10–15 s.

The FCS autocorrelation function of Alexa Fluor 488-actin in live fragments decays with a half-life time ranging between 0.7 and 2 ms (Figure 4B). The labeled actin resides in all the actin subpopulations, including the network actin and the various diffusible subpopulations. The network actin is essentially stationary in the lab frame of reference [31], and the typical timescale for exchange between the network and the diffusible actin pool is seconds (Figure 3). As such, the fluorescence signal emanating from the network does not contribute to the decay of the correlation function over the relevant timescales ($<10^2$ ms), implying that the fluorophores in the network most likely photobleach before the start of the correlation function accumulation.

The correlation functions for labeled actin in individual fragments (Figure 4B) should thus reflect the cumulative contribution from all the diffusing actin subpopulations, including monomers, monomers associated with different actin-binding proteins, and short pieces of filamentous actin of different lengths (oligomers). The diffusion time of actin monomers, monomers with different binding partners, as well as very short oligomers should be comparable (because the diffusion time of globular particles is approximately volume$^{1/3}$), whereas longer oligomers are expected to diffuse more slowly. The observed normalized correlation functions exhibit considerable heterogeneity between different fragments (Figure 4B). This variation could arise from heterogeneity in the lamellipodial environment among individual fragments (due to differences in cytoplasmic viscosity and/or network density), or from differences in the relative proportion of monomers and oligomers of different sizes. Because it is hard to separate the influence of the environment, it is difficult to infer the size distribution of diffusible actin species from these measurements. Nevertheless, because monomers (with or without binding partners) are probably the most abundant component of the diffusible actin pool, we can use these results to obtain a (lower-bound) estimate for the effective diffusion coefficient of actin monomers in the lamellipodium. To that end, we fit the correlation function from individual fragments to a simple 2D diffusion model. The measured correlation functions can be fit reasonably well with this model (Figure S3; STAR Methods), giving diffusion times of 0.7–2 ms (for a spot size of radius w_{xy} = 0.29 μm; Figure 4C). This translates to effective diffusion coefficients ranging between 10 and 30 μm^2/s, with an average value of D = 15 ± 8 μm^2/s (mean ± SD; N = 6). These values are comparable to the results of previous studies that measured actin diffusion coefficients in cells in the range of 3–30 μm^2/s [18, 37–40].

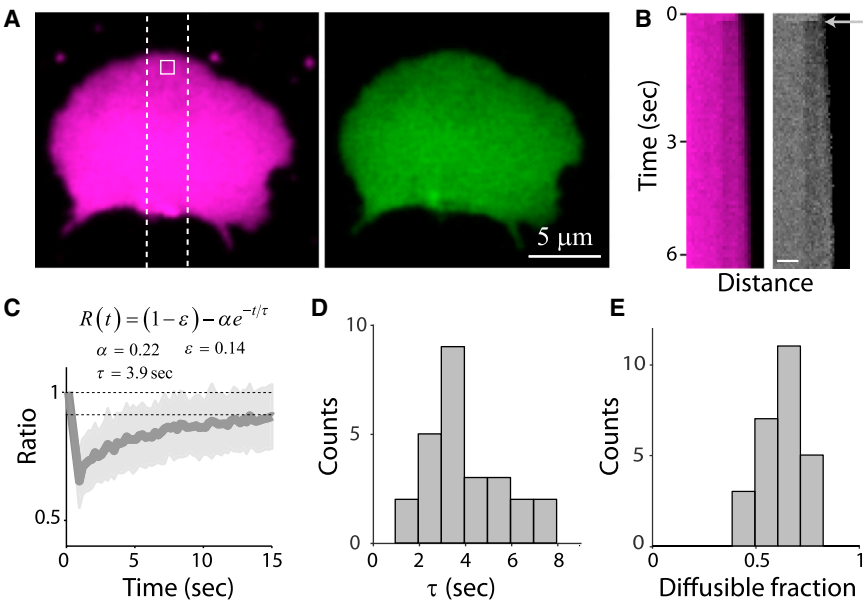

Figure 3. FRAP Analysis of Lamellipodial Actin Turnover

(A) Confocal images of a live fragment electroporated with two types of labeled actin, Alexa Fluor 647-actin (magenta) and Alexa Fluor 488-actin (green). An ~1 μm^2 region (ROI) at the center of the lamellipodium, positioned near the leading edge (white box), is bleached in one channel, and the other channel is used as a reference. A strip perpendicular to the leading edge (dashed region) is imaged as a function of time in both channels.

(B) Kymographs showing the intensity as a function of time along a line perpendicular to the leading edge for the fragment shown in (A). The bleached channel (magenta; Alexa Fluor 647-actin) and the ratio between the bleached channel and the control channel (gray; Alexa Fluor 647-actin/Alexa Fluor 488-actin) are depicted. The arrow indicates the time of bleaching. Scale bar, 2 μm.

(C) The ROI ratio intensity (Alexa Fluor 647-actin/Alexa Fluor 488-actin) as a function of time after bleaching is measured in individual fragments and normalized by setting the pre-bleach value to 1. The average normalized ROI ratio intensity from a population of fragments (N = 26) is plotted as a function of time after bleaching (line) together with the SD (shaded region). The average recovery is fit to an exponential function, $R(t) = (1 - \varepsilon) - \alpha \cdot e^{-t/\tau}$, with $\tau, \alpha, \varepsilon$ as fit parameters (top).

(D) ROI ratio intensity profiles from individual fragments are fit to an exponential as in (C). A histogram of the fitted recovery times (τ) from individual fragments is depicted. The average recovery time is 4.0 ± 1.6 s (mean ± SD; N = 26).

(E) The drop in the ROI ratio intensity (ΔR) between the pre-bleach value (1) and the first frame after bleaching reflects the fraction of network actin. A histogram of the fraction of diffusible actin ($1 - \Delta R$) in a population of fragments is shown. The average diffusible actin fraction determined from the FRAP experiments is 0.62 ± 0.11 (mean ± SD; N = 26).

See also Figure S2.

To discriminate between oligomers and monomers in the diffusible actin pool, we perform additional FCS experiments using Alexa Fluor 488-phalloidin as an actin filament-binding probe. Phalloidin binds the cleft between two adjacent actin subunits within a filament, and is therefore a highly specific probe for filamentous actin with negligible affinity to actin monomers [41]. The association of phalloidin with a much larger actin filament slows its diffusion considerably, allowing the detection of oligomers despite the presence of a large population of actin monomers [42]. Within the lamellipodium, phalloidin will be mostly bound to filaments (network filaments or diffusing filaments), due to its high affinity and the huge molar excess of filamentous actin (phalloidin:actin <1:10^3). The network-bound probe will bleach (as in the actin measurements), because the network dynamics are slow (timescales of approximately seconds), and the kinetics of phalloidin unbinding are even slower. Thus, the fluorescence correlation signal for Alexa Fluor 488-phalloidin is expected to be dominated by the dynamics of diffusing filaments. The phalloidin correlation function decays more slowly than labeled actin (Figures 4B and 4C), indicating the presence of mobile actin filaments, whose diffusion is considerably slower than that of actin monomers. By fitting the correlation function from individual fragments to a simple 2D diffusion model (Figure S3), we estimate the effective diffusion coefficient for oligomers to be ~5 ± 1 $\mu m^2/s$ (mean ± SD; N = 9), which is approximately 3-fold smaller than the monomer diffusion coefficient (Figure 4C). A rough estimate of the average oligomer length from this measurement is ~35 nm (~13 subunits; STAR Methods). This estimate is comparable to in vitro data showing that actin filaments are severed into ~20-subunit-long fragments, before breaking up into monomers [25].

Control experiments with the same dye lacking the actin filament-binding phalloidin group showed that its diffusion time in the lamellipodium (134 ± 10 μs) is more than an order of magnitude faster than Alexa Fluor 488-phalloidin (4 ± 1 × 10^3 μs; Figures 4B and 4C). The considerably slower diffusion of Alexa Fluor 488-phalloidin, together with the known specificity of phalloidin for filamentous actin, strongly argues that the FCS experiments with phalloidin report the dynamics of short, mobile actin filaments (oligomers), which are not associated with the network.

After establishing the presence of diffusing actin oligomers in the lamellipodium, we sought to measure their abundance. As explained above, the correlation signal of Alexa Fluor 488-phalloidin is dominated by the signal from phalloidin-bound diffusing oligomers, allowing us to measure the concentration of labeled oligomers in the lamellipodium. However, because the labeling fraction varies between fragments, to infer the concentration of diffusing oligomers (labeled and unlabeled) from these measurements, we need to calibrate the total amount of label in each fragment. To that end, we used quantitative densitometry to measure the total fluorescent phalloidin signal (which is mostly filament bound) in each fragment, immediately before performing FCS analysis (STAR Methods). To determine the abundance of oligomers, we take the ratio of the FCS count rate that emanates primarily from labeled diffusing filaments and the total signal (Figure 4D; STAR Methods). We find that the average mobile filament fraction in fragments is 21% ± 9% (mean ± SD; N = 26).

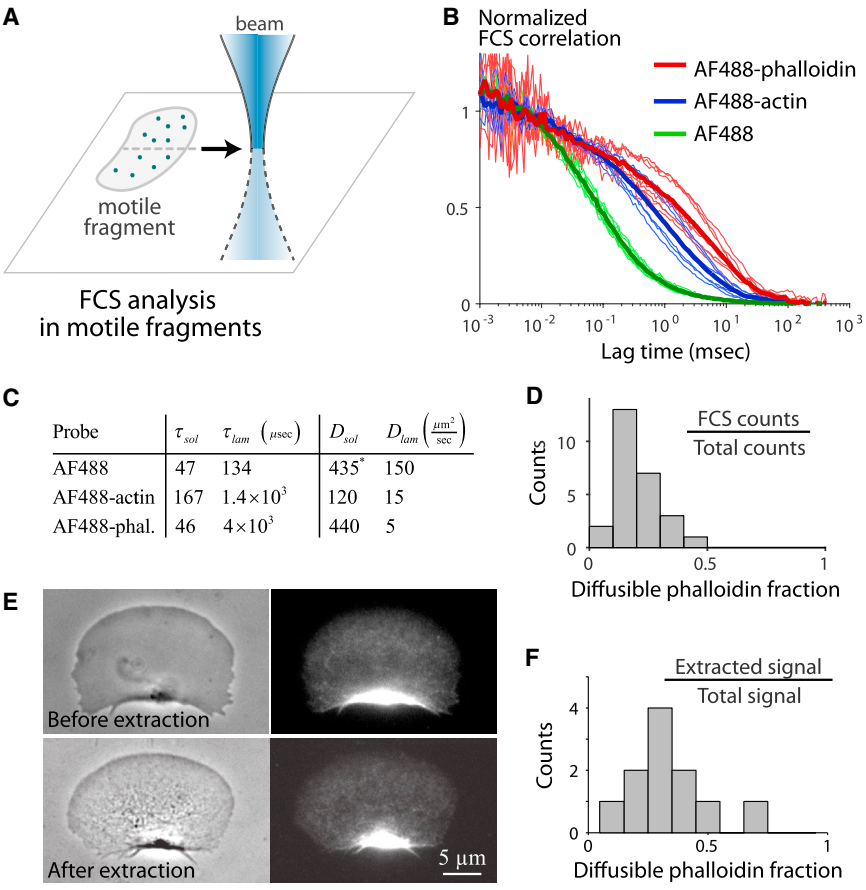

Figure 4. The Diffusible Actin Pool Contains Monomers and Oligomers

(A) A schematic illustration of the FCS experiments. A fluorescent probe is present at low concentration in a motile fragment. FCS analysis is done by positioning a laser beam in front of the center of the leading edge of the fragment, so that as the fragment moves forward the beam crosses its lamellipodium, along a line perpendicular to the leading edge.

(B) The normalized FCS correlation as a function of lag time is depicted for the different probes used: Alexa Fluor 488-actin, Alexa Fluor 488-phalloidin, and Alexa Fluor 488. The normalized correlation functions measured in individual fragments (thin lines) are shown together with the average correlation (thick lines) for each probe.

(C) The average diffusion times and effective diffusion coefficients determined from the FCS experiments for each probe. The values are determined by fitting the normalized correlation function to a simple diffusion model in solution (3D) and in the lamellipodium (2D). The asterisk indicates that this value is taken from the literature as explained in the STAR Methods.

(D) The diffusible filament fraction is determined from the FCS experiments with Alexa Fluor 488-phalloidin, as the ratio between the FCS count rate (due to diffusing phalloidin-bound filaments) and the total count rate (from all phalloidin-labeled filaments) inferred from the average lamellipodial fluorescence intensity (STAR Methods). A histogram of the fraction of diffusible phalloidin is depicted. The average fraction of diffusible filaments from the total filamentous actin pool in fragments is 0.21 ± 0.9 (mean ± SD; N = 26).

(E) Phase-contrast and fluorescence images showing the distribution of Alexa Fluor 546-phalloidin in the same fragment, before (top) and after extraction (bottom). The diffusible phalloidin fraction, which includes phalloidin-bound actin oligomers, is removed during the extraction step.

(F) The diffusible filament fraction is determined as the ratio between the integrated extracted phalloidin signal (difference between the signal before and after extraction) and the integrated signal before extraction (STAR Methods). A histogram of the fraction of diffusible filaments from the total filamentous actin pool in the fragments is depicted. The average diffusible phalloidin fraction determined from the extraction experiments is 0.32 ± 0.18 (mean ± SD; N = 11).

See also Figure S3.

We obtain an independent estimate for the fraction of mobile filaments from extraction experiments. In this case, we use phalloidin as a filament-binding probe to discriminate between filaments associated with the network and diffusing filaments. We introduce low levels of phalloidin into fragments by electroporation and compare the amount of signal before and after extraction (STAR Methods). The phalloidin signal before extraction reflects the distribution of all filamentous actin, whereas the signal after extraction is only due to network filaments (Figure 4E). We find that on average 32% ± 18% (mean ± SD; N = 11) of the phalloidin is extracted, while the remaining fraction is bound to the network (Figure 4F). The fraction of diffusible actin filaments deduced from the extraction experiments is thus comparable to the results obtained from FCS experiments in live fragments (Figure 4D).

A Model of Actin Turnover in the Lamellipodium

To understand the basic nature of actin turnover in the lamellipodium, we first analyze the implications of our measurements with regard to the kinetics of transitions between the total amounts of four subpopulations of actin (Figure 5A; STAR Methods). Namely, we consider the average concentrations of polymerizable monomers (g), non-polymerizable monomers (G), oligomers (f), and network actin (F). We assume that network actin disassembles into oligomers, which break up into monomers, which in turn can switch between a polymerizable and a non-polymerizable form (Figure 5A). The average concentrations for the four subpopulations (F, f, G, and g) can be determined based on our results and the assumption that the assembly rate of polymerizable monomers in vivo is similar to the rates measured in vitro. Because we know the amount of filamentous actin in absolute numbers (Figures 1A–1C), we can infer the concentrations of the four actin subpopulations: $F \approx 800$ μM, $f \approx 400$ μM, $G \approx 1{,}200$ μM, and $g \approx 20$ μM (Figure 5A).

To specify the model, we need the effective reaction rates for network disassembly (r), oligomer disassembly (c), monomer assembly (a), and the transitions between polymerizable and non-polymerizable monomers, β and k. We directly measure only one of these rates, $r \approx 0.25$/s (Figure 3). However, we can infer the other rates from flux balance analysis and the assumption that the rate of actin-thymosin dissociation, assumed to mediate the transition of monomers from the non-polymerizable

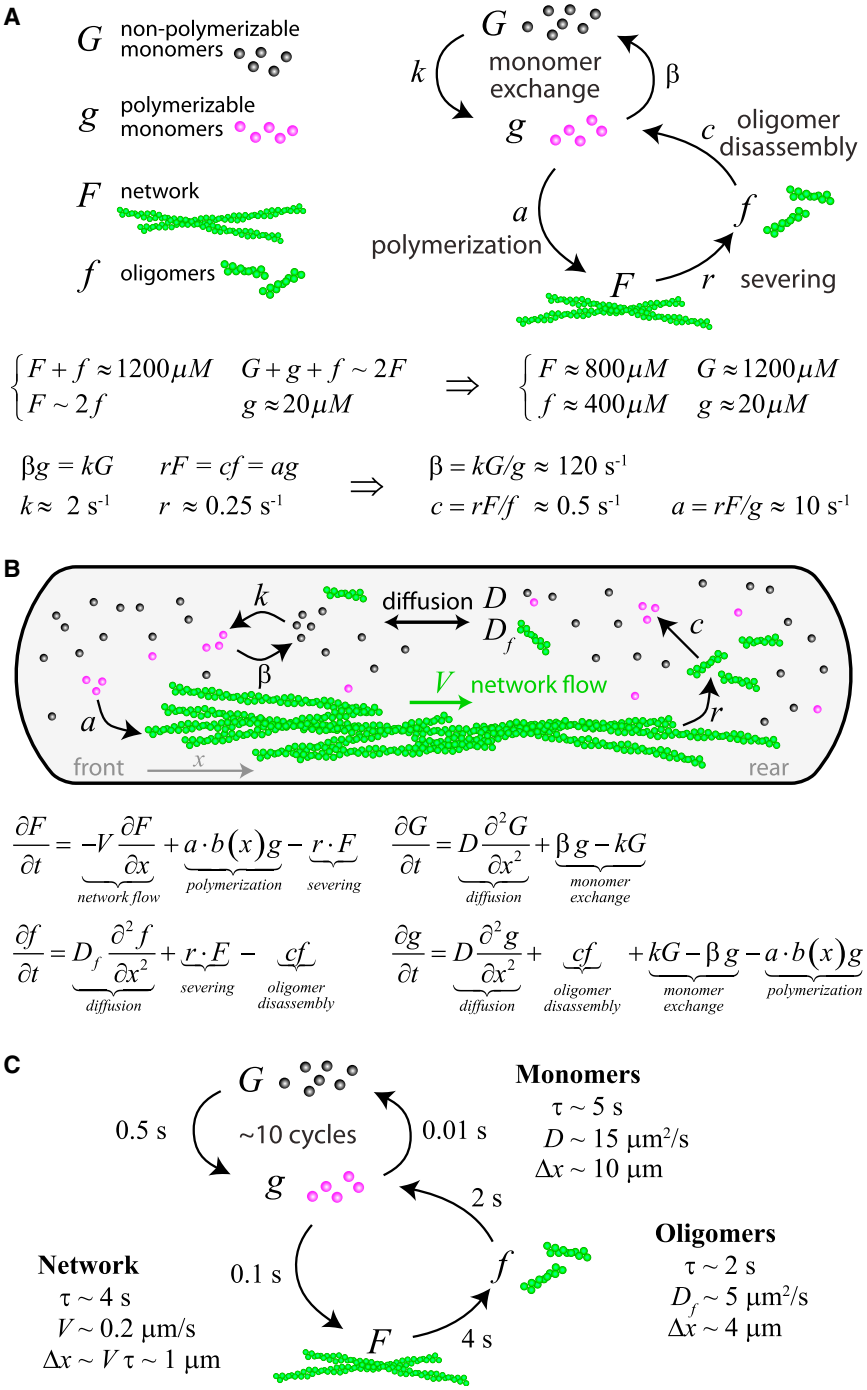

Figure 5. Mathematical Model for Lamellipodial Actin Turnover

(A) Schematic illustration of the reactions involved in lamellipodial actin turnover between the different actin subpopulations: polymerizable actin monomers assemble onto uncapped barbed ends in the network, network severing yields oligomers, oligomers disassemble into polymerizable actin monomers, and monomers exchange between polymerizable and non-polymerizable forms (top). At steady state, the system has to exhibit flux balance. This allows us to infer the average bulk concentration of each actin subpopulation and the relevant reaction rates (bottom).

(B) Schematic illustration of the mathematical model for actin turnover in fragments (top) and its formulation in terms of reaction-drift-diffusion equations in one dimension (bottom). The equations describe the time evolution of the spatial concentrations of the actin subpopulations, incorporating the reactions described in (A) and taking into account actin network flow and the diffusion of monomers and oligomers.

(C) Schematic illustration of the life cycle of an actin subunit based on the model.

See also Figures S4 and S5.

to the polymerizable pool, is the same as that measured in vitro [43, 44] (Figure 5A).

To study the spatial actin densities, we consider a 1D reaction-diffusion-drift model (Figure 5B), incorporating the measured rearward drift of the actin network (V) and diffusion of oligomers (D_f) and monomers (D). The model equations' numerical solution gives the spatial distributions of the network actin, the diffusible oligomers, and the polymerizable and non-polymerizable monomers along the anterior-posterior direction (Figure 6A). The main model prediction is that the steady-state density of diffusible actin is nearly uniform. This can be understood intuitively if we consider the relative rates of reactions, diffusion, and drift in the system (Figure 5C). The time an actin subunit spends between disassembly from the network and its subsequent assembly (~5 s), during which it undergoes multiple cycles of thymosin binding and unbinding, is comparable to the time required for a monomer to diffuse across the lamellipodium ($\tau_D = L^2 / 2D \sim (10\mu m)^2 / 2 \cdot 15\mu m^2/s \sim 3$ s). Diffusive transport is therefore responsible for establishing a uniform monomer concentration. The details of the biochemical reactions within the diffusible actin pool do not matter here; as long as a large fraction of the diffusible actin is unavailable for polymerization, and the exchange between the polymerizable and non-polymerizable pools is fast, actin subunits will diffuse across the entire lamellipodium before reassembling into the network, and all the model predictions hold (STAR Methods).

To test and confirm this model prediction, the spatial distribution of the diffusible actin can be determined experimentally from the actin extraction experiments (Figure 1D). We use a small dextran probe as a volume marker in addition to actin to correct for local variations in lamellipodial height (STAR Methods), and show that the diffusible actin fraction indeed has nearly uniform concentration (Figure 6B). The model also reproduces fairly well the observed distribution of network actin, decreasing away

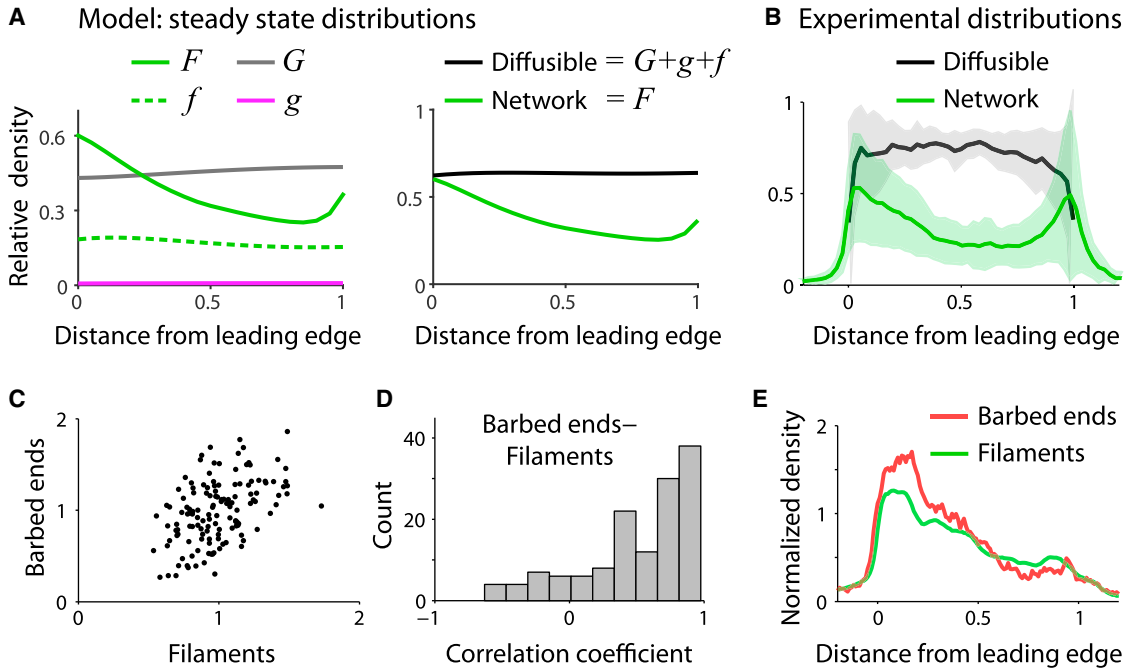

Figure 6. Model Predictions and Their Experimental Testing

(A) The model predicted steady-state distributions for the four actin subpopulations (left), and the distributions of diffusible actin, $G + g + f$, and network actin, F (right), are plotted as a function of position along the front-to-rear axis.

(B) The measured diffusible actin concentration and network density in fragments as obtained from extraction experiments (Figures 1D and 1E). The diffusible actin concentration is determined by locally subtracting the network actin density (after extraction) from the total actin density (before extraction) and dividing by the local volume marker intensity (Texas red 3 kDa dextran) to correct for height variations (N = 11). To compare to the 1D model, the relative actin distributions are determined by setting the average total actin along the cross-section to be 1. The observed diffusible and network actin density distributions (mean [lines] ± SD [shaded regions]) are comparable to the model-predicted distributions shown in (A).

(C–E) Experimental analysis of the correlation between filamentous actin and uncapped barbed ends based on co-staining of filaments and uncapped filament ends (Figure 2).

(C) Scatterplot of the average uncapped barbed end labeling intensity (rhodamine-actin) versus the average filamentous actin signal (Alexa Fluor 680-phalloidin) from individual fragments (N = 137). A clear correlation between the level of uncapped barbed ends and the level of filaments is observed.

(D and E) The spatial correlation between the filamentous actin signal and the uncapped barbed end labeling intensity along a cross-section from front to rear is examined in individual fragments.

(D) A histogram of the correlation coefficients computed in individual fragments is depicted. The vast majority of fragments (116 out of 137) exhibit positive correlation between the uncapped barbed ends and the filamentous actin distributions.

(E) The spatial distribution of the filamentous actin signal and the uncapped barbed end labeling as a function of distance from the leading edge are plotted for the fragment that exhibits the highest correlation (0.98).

from the leading edge and accumulating at the very rear (Figure 6B). The model further predicts that the network actin density can be approximately estimated as $F(x) \approx (ag/r)b(x)$ (STAR Methods). Because the monomer concentration (g) is almost uniform, the network actin distribution should be proportional to the distribution of the uncapped barbed ends, $F(x) \propto b(x)$. The observed correlation between the average amounts of network actin and uncapped barbed ends in a population of fragments (Figure 6C), as well as the spatial correlation between the network actin and uncapped barbed end distributions within individual fragments (Figures 6D and 6E), confirms this prediction.

To reveal the organizing principles of actin turnover in lamellipodia, we numerically simulate the system's response to changes in actin network dynamics in space and time in the presence and absence of the vast non-polymerizable diffusible actin pool (Figure S6; STAR Methods). We find that the rapid exchange with the large non-polymerizable pool buffers temporal fluctuations in the network assembly rate (Figure S6B), yet the cell is able to respond to internal or external cues within seconds, thanks to the rapid (approximately a few seconds) diffusive transport of dissociated actin subunits (Figure S6C). Finally, the proposed model makes it possible for a cell to rapidly increase the total amount of network actin if needed, without compromising the concentration of polymerizable monomers or cell speed, by unloading some of the reserve non-polymerizable monomer pool into the network.

DISCUSSION

To achieve quantitative understanding of actin turnover, we utilize rapidly moving lamellipodial fragments that are geometrically simple, structurally homogeneous, and persistent, and measure relevant rates and concentrations in this system. We find that the lamellipodial actin network density is ~0.8 mM and decreases approximately 2-fold from front to rear (Figure 1E), conforming to earlier studies [3, 17, 31, 45] and suggesting a slow net

network disassembly rate. Our results indicate that this net disassembly rate reflects the combined effect of much faster network disassembly and reassembly occurring throughout the lamellipodium.

Both FRAP and extraction experiments show that roughly two-thirds of the actin is in the diffusible pool, so the diffusible actin concentration is ~1.6 mM. Roughly a quarter of this diffusible actin is in filamentous form as short diffusing oligomers (~400 μM, ~13 subunits). These results are aligned with earlier work [40, 42, 46], suggesting that the presence of oligomers is a general feature of cellular actin networks. These observations are also consistent with a growing body of studies on the molecular mechanisms of actin network disassembly, which highlight severing and debranching as important steps that generate oligomers as intermediates in the disassembly process [22–25, 27]. The remaining diffusible actin concentration is still orders of magnitude higher than the in vitro actin monomer concentrations required to support the observed polymerization rates, as noted previously in other cell types [17]. It is thus highly unlikely that most of the diffusible actin in cells is available for polymerization. Thus, we argue that the majority of monomers are transiently kept in a "reserve" pool, unavailable for assembly, perhaps by being sequestered by thymosin.

Our results indicate that the actin network turnover is *local*, whereas the diffusible actin transport is *global* (Figure 5C). An actin subunit typically travels in the network ~1 μm before dissociating. The front-to-rear width of the fragment is an order of magnitude longer than this, so every part of the network undergoes ~10 cycles of reassembly across the lamellipodium. In contrast, actin subunits typically diffuse across the entire lamellipodium before reassembling into the network. This combination of local network turnover and global transport of dissociated subunits through the cytoplasm makes actin transport robust yet rapidly adaptable and amenable to regulation (Figure S6; STAR Methods). We note that in the case of larger cells, estimates that led to these conclusions will have to be reexamined.

Actin turnover in motile cells has been the subject of intense studies for decades, yet the underlying organizing principles have remained elusive. In this study, by focusing on lamellipodial fragments as a relatively simple model system, we are able to put forward a realistic, whole-lamellipodial model for actin turnover. This model, characterized by local actin network turnover and global diffusive transport, is extremely robust to the underlying biochemical details, many of which are still unknown, and reveals how the lamellipodium is able to sustain rapid protrusion while remaining responsive to external cues. Comparison with published results in many other cell types suggests that the main features of our model are relevant for lamellipodial motility across a broad range of cell types.

STAR★METHODS

Detailed methods are provided in the online version of this paper and include the following:

- KEY RESOURCES TABLE
- CONTACT FOR REAGENT AND RESOURCE SHARING
- EXPERIMENTAL MODEL AND SUBJECT DETAILS
  - Cell culture and fragment preparation
- METHOD DETAILS
  - Actin labeling
  - Quantitative filamentous actin labeling
  - Extraction experiments
  - Actin filament ends labeling
  - Microscopy
  - Fluorescence Recovery After Photobleaching (FRAP)
  - Fluorescence correlation spectroscopy (FCS)
  - Estimate of oligomer size from FCS results
  - Quantitative image analysis
  - Modeling
- QUANTIFICATION AND STATISTICAL ANALYSIS
- DATA AND SOFTWARE AVAILABILITY

SUPPLEMENTAL INFORMATION

Supplemental Information includes six figures and supplemental text and can be found with this article online at http://dx.doi.org/10.1016/j.cub.2017.08.066.

AUTHOR CONTRIBUTIONS

D.R.-B.A., N.O., K.K., and A.M. conceived and designed the experiments and the model. D.R.-B.A., N.O., E.A.-S., and K.K. performed the experiments. D.R.-B.A., N.O., O.K., and K.K. analyzed the experimental data. A.M. and J.A. developed the mathematical model and performed model simulations. K.K. and A.M. wrote the manuscript, and all the authors commented on it.

ACKNOWLEDGMENTS

We thank Erez Braun and Tzer Han Tan for comments on the manuscript. We thank Gidi Ben Yoseph for technical help and support. We thank Nitsan Dahan from the LS&E Imaging and Microscopy Unit for help with the FRAP and FCS experiments. We thank Liora Garion for her help with some of the experiments. This work was supported by a Levi Eshkol fellowship from the Israel Science Ministry (to N.O.), United States-Israel Binational Science Foundation grant number 2013275 (to K.K. and A.M.), and NIH grant number GM068952 (to A.M.).

Received: August 22, 2016
Revised: July 21, 2017
Accepted: August 29, 2017
Published: September 28, 2017

REFERENCES

1. Pollard, T.D., and Borisy, G.G. (2003). Cellular motility driven by assembly and disassembly of actin filaments. Cell *112*, 453–465.
2. Blanchoin, L., Boujemaa-Paterski, R., Sykes, C., and Plastino, J. (2014). Actin dynamics, architecture, and mechanics in cell motility. Physiol. Rev. *94*, 235–263.
3. Abraham, V.C., Krishnamurthi, V., Taylor, D.L., and Lanni, F. (1999). The actin-based nanomachine at the leading edge of migrating cells. Biophys. J. *77*, 1721–1732.
4. Pollard, T.D., Blanchoin, L., and Mullins, R.D. (2000). Molecular mechanisms controlling actin filament dynamics in nonmuscle cells. Annu. Rev. Biophys. Biomol. Struct. *29*, 545–576.
5. Pollard, T.D., and Cooper, J.A. (2009). Actin, a central player in cell shape and movement. Science *326*, 1208–1212.
6. Shekhar, S., Pernier, J., and Carlier, M.-F. (2016). Regulators of actin filament barbed ends at a glance. J. Cell Sci. *129*, 1085–1091.

7. Campellone, K.G., and Welch, M.D. (2010). A nucleator arms race: cellular control of actin assembly. Nat. Rev. Mol. Cell Biol. *11*, 237–251.
8. Mullins, R.D., Heuser, J.A., and Pollard, T.D. (1998). The interaction of Arp2/3 complex with actin: nucleation, high affinity pointed end capping, and formation of branching networks of filaments. Proc. Natl. Acad. Sci. USA *95*, 6181–6186.
9. Borisy, G.G., and Svitkina, T.M. (2000). Actin machinery: pushing the envelope. Curr. Opin. Cell Biol. *12*, 104–112.
10. Svitkina, T.M., and Borisy, G.G. (1999). Arp2/3 complex and actin depolymerizing factor/cofilin in dendritic organization and treadmilling of actin filament array in lamellipodia. J. Cell Biol. *145*, 1009–1026.
11. Theriot, J.A., and Mitchison, T.J. (1992). The nucleation-release model of actin filament dynamics in cell motility. Trends Cell Biol. *2*, 219–222.
12. Watanabe, N., and Mitchison, T.J. (2002). Single-molecule speckle analysis of actin filament turnover in lamellipodia. Science *295*, 1083–1086.
13. Theriot, J.A., and Mitchison, T.J. (1991). Actin microfilament dynamics in locomoting cells. Nature *352*, 126–131.
14. Lewalle, A., Fritzsche, M., Wilson, K., Thorogate, R., Duke, T., and Charras, G. (2014). A phenomenological density-scaling approach to lamellipodial actin dynamics. Interface Focus *4*, 20140006.
15. Vitriol, E.A., McMillen, L.M., Kapustina, M., Gomez, S.M., Vavylonis, D., and Zheng, J.Q. (2015). Two functionally distinct sources of actin monomers supply the leading edge of lamellipodia. Cell Rep. *11*, 433–445.
16. Lai, F.P.L., Szczodrak, M., Block, J., Faix, J., Breitsprecher, D., Mannherz, H.G., Stradal, T.E.B., Dunn, G.A., Small, J.V., and Rottner, K. (2008). Arp2/3 complex interactions and actin network turnover in lamellipodia. EMBO J. *27*, 982–992.
17. Koestler, S.A., Rottner, K., Lai, F., Block, J., Vinzenz, M., and Small, J.V. (2009). F- and G-actin concentrations in lamellipodia of moving cells. PLoS ONE *4*, e4810.
18. Kiuchi, T., Nagai, T., Ohashi, K., and Mizuno, K. (2011). Measurements of spatiotemporal changes in G-actin concentration reveal its effect on stimulus-induced actin assembly and lamellipodium extension. J. Cell Biol. *193*, 365–380.
19. Cramer, L.P., Briggs, L.J., and Dawe, H.R. (2002). Use of fluorescently labelled deoxyribonuclease I to spatially measure G-actin levels in migrating and non-migrating cells. Cell Motil. Cytoskeleton *51*, 27–38.
20. Lee, C.W., Vitriol, E.A., Shim, S., Wise, A.L., Velayutham, R.P., and Zheng, J.Q. (2013). Dynamic localization of G-actin during membrane protrusion in neuronal motility. Curr. Biol. *23*, 1046–1056.
21. Van Goor, D., Hyland, C., Schaefer, A.W., and Forscher, P. (2012). The role of actin turnover in retrograde actin network flow in neuronal growth cones. PLoS ONE *7*, e30959.
22. Kueh, H.Y., Charras, G.T., Mitchison, T.J., and Brieher, W.M. (2008). Actin disassembly by cofilin, coronin, and Aip1 occurs in bursts and is inhibited by barbed-end cappers. J. Cell Biol. *182*, 341–353.
23. Staiger, C.J., Sheahan, M.B., Khurana, P., Wang, X., McCurdy, D.W., and Blanchoin, L. (2009). Actin filament dynamics are dominated by rapid growth and severing activity in the *Arabidopsis* cortical array. J. Cell Biol. *184*, 269–280.
24. Johnston, A.B., Collins, A., and Goode, B.L. (2015). High-speed depolymerization at actin filament ends jointly catalysed by Twinfilin and Srv2/CAP. Nat. Cell Biol. *17*, 1504–1511.
25. Jansen, S., Collins, A., Chin, S.M., Ydenberg, C.A., Gelles, J., and Goode, B.L. (2015). Single-molecule imaging of a three-component ordered actin disassembly mechanism. Nat. Commun. *6*, 7202.
26. Haviv, L., Gillo, D., Backouche, F., and Bernheim-Groswasser, A. (2008). A cytoskeletal demolition worker: myosin II acts as an actin depolymerization agent. J. Mol. Biol. *375*, 325–330.
27. Wilson, C.A., Tsuchida, M.A., Allen, G.M., Barnhart, E.L., Applegate, K.T., Yam, P.T., Ji, L., Keren, K., Danuser, G., and Theriot, J.A. (2010). Myosin II contributes to cell-scale actin network treadmilling through network disassembly. Nature *465*, 373–377.
28. Brieher, W. (2013). Mechanisms of actin disassembly. Mol. Biol. Cell *24*, 2299–2302.
29. Ponti, A., Machacek, M., Gupton, S.L., Waterman-Storer, C.M., and Danuser, G. (2004). Two distinct actin networks drive the protrusion of migrating cells. Science *305*, 1782–1786.
30. Verkhovsky, A.B., Svitkina, T.M., and Borisy, G.G. (1999). Self-polarization and directional motility of cytoplasm. Curr. Biol. *9*, 11–20.
31. Ofer, N., Mogilner, A., and Keren, K. (2011). Actin disassembly clock determines shape and speed of lamellipodial fragments. Proc. Natl. Acad. Sci. USA *108*, 20394–20399.
32. Laurent, V.M., Kasas, S., Yersin, A., Schäffer, T.E., Catsicas, S., Dietler, G., Verkhovsky, A.B., and Meister, J.-J. (2005). Gradient of rigidity in the lamellipodia of migrating cells revealed by atomic force microscopy. Biophys. J. *89*, 667–675.
33. Urban, E., Jacob, S., Nemethova, M., Resch, G.P., and Small, J.V. (2010). Electron tomography reveals unbranched networks of actin filaments in lamellipodia. Nat. Cell Biol. *12*, 429–435.
34. Svitkina, T. (2007). Electron microscopic analysis of the leading edge in migrating cells. Methods Cell Biol. *79*, 295–319.
35. Symons, M.H., and Mitchison, T.J. (1991). Control of actin polymerization in live and permeabilized fibroblasts. J. Cell Biol. *114*, 503–513.
36. Ofer, N., Abu Shah, E., and Keren, K. (2014). Differential mapping of the free barbed and pointed ends of actin filaments in cells. Cytoskeleton *71*, 341–350.
37. McGrath, J.L., Tardy, Y., Dewey, C.F., Jr., Meister, J.J., and Hartwig, J.H. (1998). Simultaneous measurements of actin filament turnover, filament fraction, and monomer diffusion in endothelial cells. Biophys. J. *75*, 2070–2078.
38. Zicha, D., Dobbie, I.M., Holt, M.R., Monypenny, J., Soong, D.Y.H., Gray, C., and Dunn, G.A. (2003). Rapid actin transport during cell protrusion. Science *300*, 142–145.
39. McDonald, D., Carrero, G., Andrin, C., de Vries, G., and Hendzel, M.J. (2006). Nucleoplasmic beta-actin exists in a dynamic equilibrium between low-mobility polymeric species and rapidly diffusing populations. J. Cell Biol. *172*, 541–552.
40. Smith, M.B., Kiuchi, T., Watanabe, N., and Vavylonis, D. (2013). Distributed actin turnover in the lamellipodium and FRAP kinetics. Biophys. J. *104*, 247–257.
41. Estes, J.E., Selden, L.A., and Gershman, L.C. (1981). Mechanism of action of phalloidin on the polymerization of muscle actin. Biochemistry *20*, 708–712.
42. Gowrishankar, K., Ghosh, S., Saha, S., C., R., Mayor, S., and Rao, M. (2012). Active remodeling of cortical actin regulates spatiotemporal organization of cell surface molecules. Cell *149*, 1353–1367.
43. Pollard, T.D. (1986). Rate constants for the reactions of ATP- and ADP-actin with the ends of actin filaments. J. Cell Biol. *103*, 2747–2754.
44. Dufort, P.A., and Lumsden, C.J. (1996). How profilin/barbed-end synergy controls actin polymerization: a kinetic model of the ATP hydrolysis circuit. Cell Motil. Cytoskeleton *35*, 309–330.
45. Keren, K., Pincus, Z., Allen, G.M., Barnhart, E.L., Marriott, G., Mogilner, A., and Theriot, J.A. (2008). Mechanism of shape determination in motile cells. Nature *453*, 475–480.
46. Watts, R.G., and Howard, T.H. (1993). Mechanisms for actin reorganization in chemotactic factor-activated polymorphonuclear leukocytes. Blood *81*, 2750–2757.
47. Petrásek, Z., and Schwille, P. (2008). Precise measurement of diffusion coefficients using scanning fluorescence correlation spectroscopy. Biophys. J. *94*, 1437–1448.
48. Spudich, J.A., Huxley, H.E., and Finch, J.T. (1972). Regulation of skeletal muscle contraction. II. Structural studies of the interaction of the tropomyosin-troponin complex with actin. J. Mol. Biol. *72*, 619–632.
49. Berg, H.C. (1993). Random Walks in Biology (Princeton University Press).

50. Sakha, F., and Fazli, H. (2010). Three-dimensional Brownian diffusion of rod-like macromolecules in the presence of randomly distributed spherical obstacles: molecular dynamics simulation. J. Chem. Phys. *133*, 234904.
51. Pincus, Z., and Theriot, J.A. (2007). Comparison of quantitative methods for cell-shape analysis. J. Microsc. *227*, 140–156.
52. Wang, Y.L. (1985). Exchange of actin subunits at the leading edge of living fibroblasts: possible role of treadmilling. J. Cell Biol. *101*, 597–602.
53. Zigmond, S.H. (1993). Recent quantitative studies of actin filament turnover during cell locomotion. Cell Motil. Cytoskeleton *25*, 309–316.
54. Mogilner, A., and Edelstein-Keshet, L. (2002). Regulation of actin dynamics in rapidly moving cells: a quantitative analysis. Biophys. J. *83*, 1237–1258.
55. Lieber, A.D., Schweitzer, Y., Kozlov, M.M., and Keren, K. (2015). Front-to-rear membrane tension gradient in rapidly moving cells. Biophys. J. *108*, 1599–1603.
56. Kovar, D.R., and Pollard, T.D. (2004). Insertional assembly of actin filament barbed ends in association with formins produces piconewton forces. Proc. Natl. Acad. Sci. USA *101*, 14725–14730.
57. Prass, M., Jacobson, K., Mogilner, A., and Radmacher, M. (2006). Direct measurement of the lamellipodial protrusive force in a migrating cell. J. Cell Biol. *174*, 767–772.
58. Keren, K., Yam, P.T., Kinkhabwala, A., Mogilner, A., and Theriot, J.A. (2009). Intracellular fluid flow in rapidly moving cells. Nat. Cell Biol. *11*, 1219–1224.
59. Garcia, A.L. (1999). Numerical Methods for Physics, Second Edition, R. Alison, and F.C. Paul, eds. (Prentice-Hall).
60. Courtemanche, N., Lee, J.Y., Pollard, T.D., and Greene, E.C. (2013). Tension modulates actin filament polymerization mediated by formin and profilin. Proc. Natl. Acad. Sci. USA *110*, 9752–9757.
61. Roland, J., Berro, J., Michelot, A., Blanchoin, L., and Martiel, J.-L. (2008). Stochastic severing of actin filaments by actin depolymerizing factor/cofilin controls the emergence of a steady dynamical regime. Biophys. J. *94*, 2082–2094.
62. Reymann, A.-C., Suarez, C., Guérin, C., Martiel, J.-L., Staiger, C.J., Blanchoin, L., and Boujemaa-Paterski, R. (2011). Turnover of branched actin filament networks by stochastic fragmentation with ADF/cofilin. Mol. Biol. Cell *22*, 2541–2550.
63. Hansen, S.D., and Mullins, R.D. (2015). Lamellipodin promotes actin assembly by clustering Ena/VASP proteins and tethering them to actin filaments. eLife *4*, e06585.
64. Michelot, A., Grassart, A., Okreglak, V., Costanzo, M., Boone, C., and Drubin, D.G. (2013). Actin filament elongation in Arp2/3-derived networks is controlled by three distinct mechanisms. Dev. Cell *24*, 182–195.
65. Ditlev, J.A., Vacanti, N.M., Novak, I.L., and Loew, L.M. (2009). An open model of actin dendritic nucleation. Biophys. J. *96*, 3529–3542.
66. Djafarzadeh, S., and Niggli, V. (1997). Signaling pathways involved in dephosphorylation and localization of the actin-binding protein cofilin in stimulated human neutrophils. Exp. Cell Res. *236*, 427–435.
67. Dickinson, R.B., and Purich, D.L. (2006). Diffusion rate limitations in actin-based propulsion of hard and deformable particles. Biophys. J. *91*, 1548–1563.
68. Lieber, A.D., Yehudai-Resheff, S., Barnhart, E.L., Theriot, J.A., and Keren, K. (2013). Membrane tension in rapidly moving cells is determined by cytoskeletal forces. Curr. Biol. *23*, 1409–1417.
69. Kage, F., Winterhoff, M., Dimchev, V., Mueller, J., Thalheim, T., Freise, A., Brühmann, S., Kollasser, J., Block, J., Dimchev, G., et al. (2017). FMNL formins boost lamellipodial force generation. Nat. Commun. *8*, 14832.
70. Pollard, T.D. (2007). Regulation of actin filament assembly by Arp2/3 complex and formins. Annu. Rev. Biophys. Biomol. Struct. *36*, 451–477.
71. Huber, F., Käs, J., and Stuhrmann, B. (2008). Growing actin networks form lamellipodium and lamellum by self-assembly. Biophys. J. *95*, 5508–5523.
72. Iwasa, J.H., and Mullins, R.D. (2007). Spatial and temporal relationships between actin-filament nucleation, capping, and disassembly. Curr. Biol. *17*, 395–406.
73. Hayakawa, K., Tatsumi, H., and Sokabe, M. (2011). Actin filaments function as a tension sensor by tension-dependent binding of cofilin to the filament. J. Cell Biol. *195*, 721–727.
74. Condeelis, J., and Singer, R.H. (2005). How and why does beta-actin mRNA target? Biol. Cell *97*, 97–110.
75. Yarmola, E.G., Dranishnikov, D.A., and Bubb, M.R. (2008). Effect of profilin on actin critical concentration: a theoretical analysis. Biophys. J. *95*, 5544–5573.
76. Carlier, M.F., and Pantaloni, D. (1997). Control of actin dynamics in cell motility. J. Mol. Biol. *269*, 459–467.
77. Akin, O., and Mullins, R.D. (2008). Capping protein increases the rate of actin-based motility by promoting filament nucleation by the Arp2/3 complex. Cell *133*, 841–851.
78. Mc Leod, J.F., Kowalski, M.A., and Haddad, J.G., Jr. (1989). Interactions among serum vitamin D binding protein, monomeric actin, profilin, and profilactin. J. Biol. Chem. *264*, 1260–1267.
79. White, P., and Cooke, N. (2000). The multifunctional properties and characteristics of vitamin D-binding protein. Trends Endocrinol. Metab. *11*, 320–327.
80. Hertzog, M., van Heijenoort, C., Didry, D., Gaudier, M., Coutant, J., Gigant, B., Didelot, G., Préat, T., Knossow, M., Guittet, E., and Carlier, M.F. (2004). The β-thymosin/WH2 domain: structural basis for the switch from inhibition to promotion of actin assembly. Cell *117*, 611–623.
81. Mannherz, H.G., Ballweber, E., Galla, M., Villard, S., Granier, C., Steegborn, C., Schmidtmann, A., Jaquet, K., Pope, B., and Weeds, A.G. (2007). Mapping the ADF/cofilin binding site on monomeric actin by competitive cross-linking and peptide array: evidence for a second binding site on monomeric actin. J. Mol. Biol. *366*, 745–755.
82. Roy, P., Rajfur, Z., Jones, D., Marriott, G., Loew, L., and Jacobson, K. (2001). Local photorelease of caged thymosin beta4 in locomoting keratocytes causes cell turning. J. Cell Biol. *153*, 1035–1048.
83. Dimchev, G., Steffen, A., Kage, F., Dimchev, V., Pernier, J., Carlier, M.-F., and Rottner, K. (2017). Efficiency of lamellipodia protrusion is determined by the extent of cytosolic actin assembly. Mol. Biol. Cell *28*, 1311–1325.
84. Svitkina, T.M. (2013). Ultrastructure of protrusive actin filament arrays. Curr. Opin. Cell Biol. *25*, 574–581.
85. Tsuchida, M.A. (2012) Dynamics and mechanics of the actin cytoskeleton ex vivo. PhD thesis (Stanford University).
86. Cooper, J.A. (2002). Actin dynamics: tropomyosin provides stability. Curr. Biol. *12*, R523–R525.
87. Rosenblatt, J., Peluso, P., and Mitchison, T.J. (1995). The bulk of unpolymerized actin in *Xenopus* egg extracts is ATP-bound. Mol. Biol. Cell *6*, 227–236.
88. Aguda, A.H., Xue, B., Irobi, E., Préat, T., and Robinson, R.C. (2006). The structural basis of actin interaction with multiple WH2/beta-thymosin motif-containing proteins. Structure *14*, 469–476.
89. Okreglak, V., and Drubin, D.G. (2010). Loss of Aip1 reveals a role in maintaining the actin monomer pool and an in vivo oligomer assembly pathway. J. Cell Biol. *188*, 769–777.
90. Xue, B., and Robinson, R.C. (2013). Guardians of the actin monomer. Eur. J. Cell Biol. *92*, 316–332.

STAR★METHODS

KEY RESOURCES TABLE

REAGENT or RESOURCE	SOURCE	IDENTIFIER
Chemicals, Peptides, and Recombinant Proteins		
Leibovitz's L-15 medium	GIBCO-BRL	21083027
Fetal bovine serum (FBS)	Invitrogen	10270106
antibiotic-antimycotic (ABAM)	Sigma Aldrich	A5955
trypsin	GIBCO-BRL	25050014
staurosporine	Sigma Aldrich	S4400
16% formaldehyde	Belgar	32120132
phosphate buffer saline (PBS)	GIBCO	70011036
Triton X-100	Sigma Aldrich	T9284
Polyethylenglycol (PEG) 35000MW	Sigma Aldrich	81310
Albumin Bovine Fraction V powder (BAS)	Sigma Aldrich	A7906
Actin protein: chicken skeletal muscle	This study	
capping protein	This study	Mouse $\alpha 1\beta 2$ capping protein, His-tagged construct from Lappalainen lab
tetramethylrhodamine iodoacetamide	Molecular Probes/Invitrogen	T6006
Alexa Fluor 488 NHS Ester (Succinimidyl Ester)	Molecular Probes/Invitrogen	A20000
Alexa Fluor 647 NHS Ester (Succinimidyl Ester)	Molecular Probes/Invitrogen	A20106
Adenosine Triphosphate - grade II	Sigma Aldrich	A3377
Phalloidin	Molecular Probes/Invitrogen	P3457
Alexa FLuoro 680 Phalloidin 300U	Molecular Probes/Invitrogen	A22286
Alexa FLuoro 546 Phalloidin 300U	Molecular Probes/Invitrogen	A22283
Alexa FLuoro 488 Phalloidin 300U	Molecular probes/Invitrogen	A12379
3kD Alexa FLuoro 488-Dextran	Molecular Probes/Invitrogen	D34682
VectaMount Permanent Mounting Medium	Vector labs	H-5000
Experimental Models: Organisms/Strains		
Central American cichlid *H. nicaraguensis*	Tangled Up in Cichlids	http://www.tangledupincichlids.com/
Software and Algorithms		
MATLAB	The MathWorks	N/A
CellTool	Zach Pincus	http://zplab.wustl.edu/celltool/

CONTACT FOR REAGENT AND RESOURCE SHARING

Further information and requests for resources and reagents should be directed to and will be fulfilled by the Lead Contact, Kinneret Keren (kinneret@physics.technion.ac.il).

EXPERIMENTAL MODEL AND SUBJECT DETAILS

Cell culture and fragment preparation

Lamellipodial fragments are prepared from primary keratocyte cultures from the Central American cichlid *H. nicaraguensis* as previously reported [31]. Scales are plucked from the fish body of healthy mature male or female fish. The scales are rinsed in enriched medium (Leibovitz's L-15 medium (GIBCO BRL), supplemented with 14.2 mM HEPES pH 7.4, 10% FBS (Invitorgen) and 1% antibiotic-antimycotic (Sigma Aldrich), sandwiched between two coverslips and incubated overnight at room temperature (RT). The cells are replated onto a glass-bottom petri dish (FluoroDish, World Precision Instruments) following treatment with trypsin (GIBCO BRL). Fragment formation is induced after several hours by treating cells with 100 nM staurosporine (Sigma) in 1 mL medium for 30 min at 35°C, with the lid half open. The cultures are then washed with normal medium and allowed to recover at RT for at least 15-30 min.

METHOD DETAILS

Actin labeling

Skeletal actin is purified from chicken skeletal muscle using standard protocols. Actin is chemically labeled with one of the following dyes, tetramethylrhodamine iodoacetamide, Alexa Fluor 488 Carboxylic Acid Succinimidyl Ester, or Alexa Fluor 647 Carboxylic Acid Succinimidyl Ester (all from Molecular Probes). The actin is labeled in filamentous form, and subsequently purified by two cycles of polymerization and depolyemrization. For FRAP, FCS and extraction experiments we use a labeling ratio of ~50%, while for ends labeling we use a labeling ratio of ~10%. The labeled actin is stored in G-buffer (10mM Tris-HCl pH 8.6, 0.1mM DTT, 0.2mM ATP, 0.1mM $CaCl_2$).

Quantitative filamentous actin labeling

Quantitative measurements of actin filament distribution in fragments are done by adding actin filaments to fixed samples as calibrated probes [3]. Actin filaments are generated by incubating 2 μM actin in G-Mg buffer (2 mM Tris-HCl pH 8, 0.5 mM DTT, 0.2 mM ATP and 0.1 mM $MgCl_2$) for 1 hr on ice, followed by the addition of 10 × F-buffer (250 mM Tris-HCl pH 8, 1 M KCL, 20 mM MgCl2, 10 mM ATP and 1 mM DTT) and allowing the polymerization process to proceed for 15 min – 1 hr at room temperature. Filaments are diluted 100 × into Phosphate Buffered Saline (PBS, GIBCO BRL) containing 0.2 μM phalloidin Alexa Fluor 546 and incubated on ice for at least 5 min. At the same time, a cell culture sample after fragment preparation is fixed with 4% formaldehyde in CBS buffer (10 mM MES pH 6.1, 117 mM KCL, 3 mM MgCl2 and 2mM EGTA, 320 mM sucrose) for 15 min, followed by 2 × PBS washes. The sample is washed once with PBS-BT (PBS, 3% BSA and 0.1% Triton X-100), incubated with PBS-BT for 5 min, washed 2 × with PBS, and then left to equilibrate in a 100 μL of the diluted stained filament solution for ~4 hr. The sample is then sandwiched by placing a 22 mm round coverslip on top and extra filament solution is absorbed gently. The coverslip is sealed with vaseline:lanolin:paraffin (at 1:1:1).

Stained fragments and filaments are imaged on the same coverslip using identical imaging conditions, except that filaments are imaged using exposure times 100 × longer. The total fluorescence intensity of an actin filament per unit length is calculated by manually taking perpendicular cross-sections of individual filaments and calculating the integrated fluorescence per unit length. The average filament intensity per unit length is determined by taking the mean value obtained from ~80 filaments on each coverslip. This value is then used to calibrate the amount of filaments per μm^2 in fragments (Figure 1C). The data shown is taken from 3 independent experiments (N~50 fragments per experiment).

Extraction experiments

Extraction experiments are done by introducing labeled probes into live fragments and imaging the same fragment before and after extraction. The probe is electroporated into cells (prior to fragmentation) using a home-made electroporator for adherent cells [31]. Following fragmentation, live electroporated fragments are identified and imaged, and then immediately extracted on the microscope stage as in [34]. Extraction is done by replacing the cell medium with extraction solution: 1% Triton X-100, 4% Polyethylenglycol (PEG) 35000MW (Sigma), 10 μM unlabeled phalloidin (Molecular Probes) in m-buffer (50mM Imidazole, 50mM KCl, 0.5mM MgCl2, 0.1mM EDTA, 0.5mM EGTA) for 3 min, and then washing with m-buffer. The same fragments are subsequently imaged again under the same conditions. For actin extractions we use an electroporation solution containing ~50μM labeled actin in G-buffer. The final cellular concentration of intracellular labeled actin is < 5μM which is < 1% of the endogenous actin. Extraction experiments with actin and volume marker are done in a similar manner, except that 3kD 488-Dextran (1 mg/ml) is added to the electroporation solution. The spatial distribution of the diffusible actin concentration is obtained by dividing the difference between the local actin signal before and after extraction by the local volume marker intensity (before extraction).

Extraction experiments with phalloidin are done with an electroporation solution containing 6 μM Alexa Fluor 546-phalloidin (Molecular Probes). To prevent phalloidin aggregation, the phalloidin is pre-mixed with 5 μM (each) dNTP nucleotides and incubated for ~15 min at RT [31]. The phalloidin concentrations used are sufficiently low to assume that the actin dynamics are not perturbed significantly, and that the majority of intracellular phalloidin is bound to filaments. The extracted fraction is calculated by subtracting the integrated fluorescence signal after extraction from the total signal before extraction.

Actin filament ends labeling

Uncapped barbed and pointed ends labeling is done as described previously [36]. Samples are briefly fixed with 4% formaldehyde in CBS buffer (see above) for 30 s. Samples are then washed with PBS-BT, and incubated with PBS-BT containing 0.2 μM Alexa Fluor 680-phallidin, 0.1 mM ATP and 2 μM rhodamine-actin monomers (staining mix) for ~60 s to label the uncapped barbed ends. This step leads to negligible labeling of uncapped pointed ends [36]. Subsequent labeling of uncapped pointed ends is done using a longer incubation time and in the presence of capping protein (to prevent further labeling of uncapped barbed ends). Samples are washed with PBS-BT, and incubated with PBS-BT containing 0.66 μM capping protein for 5 min, followed by labeling with a staining mix containing 2 μM Alexa Fluor 488-actin supplemented with 0.66 μM capping protein for 10 min. Stained samples are washed with PBS and mounted in VectaMount (Vector Labs, Burlingame, CA, USA).

Microscopy

All images are acquired on a Zeiss AxioObserver inverted microscope (Zeiss), unless indicated otherwise. Images are acquired with a CoolSnap HQ2 CCD camera (Photometrics) using a 63 × oil objective (NA = 1.4) with a 1.6 × optovar. All live cell imaging is performed in enriched medium (see above) at RT.

Fluorescence Recovery After Photobleaching (FRAP)

Cells are electroporated as above with two types of labeled actin monomers, Alexa Fluor 647-actin and Alexa Fluor 488-actin, which are mixed in the electroporation solution at ~40 μM each. One label is bleached and the other is used as a reference for tracking inherent variation of actin density. The total amount of labeled actin introduced into fragments is < 8 μM, which is < 1% of the endogenous actin pool. Following electroporation, fragmentation is induced as above. Before imaging, the samples are immersed in 2 mL enriched medium that has been degassed overnight by slowly bubbling nitrogen, and supplemented with 10 mM D-succinate (in 0.2M HEPES ph 7) and 12 u/ml OxiFluor (Oxyrase). The medium is then covered with mineral oil which has been degassed in vacuum overnight, to avoid fluid evaporation during the experiment.

FRAP experiment are done on a LSM 710 laser scanning confocal microscope (Zeiss), using a 63 × oil lens (NA = 1.4). A full frame scan of a fragment is first performed. Subsequently, a 128x8 pixel strip is defined perpendicular to the leading edge, so that it encompasses the central strip of the fragment from front to rear, while allowing faster acquisition rate. Imaging is done simultaneously in both channels, exciting with a 25 mW 488 nm multiline argon laser at 1%–8% power and a 5 mW 639 nm solid state laser at 0.5%–6% power, using appropriate filters. Photobleaching is done in one of the channels after 3 frames. A ~1 μm diameter region (ROI), positioned at the center of the lamellipodium, 0.5-3 μm from the leading edge, is bleached by scanning the laser beam over the region at 100% laser power for ~0.5 s. Imaging of the strip is subsequently continued for 30-45 s at 60-80 ms per frame. The bleaching dose was chosen as the lowest dose that leads to maximal levels of signal reduction. Higher bleaching doses were sometimes found to induce damage and filament breakage in the network, which could be easily identified in our experiments by enhanced polymerization (on the newly-generated filament ends) leading to an increased signal in the ROI in the control channel.

The ROI fluorescence intensity is corrected by background subtracting the average intensity of a region outside the fragment, and subsequently corrected for photobleaching by dividing the signal from the ROI by the signal from the entire frame for each time point. The fraction of diffusible actin is determined from the drop in the fluorescence intensity in the ROI in the first frame after bleaching compared to the pre-bleached signal. To account for local variations in the actin density, we consider the ratio between the corrected fluorescence intensity in the ROI in the bleached channel and the reference channel, and normalize the ratio to have a value of 1 prior to bleaching. The recovery rate is determined by fitting the normalized ratio signal to an exponential function, $R(t) = (1 - \varepsilon) - \alpha \cdot e^{-t/\tau}$, taking $\tau, \alpha, \varepsilon$ as fit parameters, where τ is the timescale for recovery, α is the fraction recovered, and ε reflects the fraction of the ratio signal that does not recover. The bleached region area is ~1 μm^2, which is < 1% of the fragment area. The decrease in signal due to a reduction in the overall amount of labeled actin in the bleached channel is hence expected to be negligible in fragments (Figure 3), and even smaller in whole cells (Figure S2). In particular, similar partial recovery is observed in FRAP experiments preformed in fragments (Figure 3C) and in whole keratocytes (Figure S2), where the total pool of labeled probe is much larger, and hence artifacts associated with bleaching a fraction of the overall labeled probe pool should be mitigated.

Fluorescence correlation spectroscopy (FCS)

FCS measurements are done using a LSM 710 laser scanning confocal microscope (Zeiss) with a Zeiss BiG detector which contains two photomultipliers with GaAsP photocathodes. Different probes are used for FCS analysis: Alexa Fluor 488, Alexa Fluor 488-phalloidin and Alexa Fluor 488-actin. All probes are excited with a 25 mW 488 nm multiline argon laser used at 0.5%–1% power. The detector afterpulsing was calibrated on a white noise signal and subtracted from the measured correlation curves. Observations are made using a 40 × (NA = 1.25) water immersion objective. Fluorescence emission is separated from the laser light using a band pass filter (525–550 nm). Each probe is calibrated prior to use by performing FCS analysis in solution. The fluorescence correlation function of each probe in solution is fit to a simple 3D diffusion model, taking into account corrections due to triplet states. The beam waist radius in our system is determined to be $w_{x-y} = 0.29 \mu m$, by fitting the fluorescence correlation function for Alexa Fluor 488, taking the measured value for its diffusion from the literature, 435 μm^2/s [47]. The beam waist determined is subsequently used when calculating the effective diffusion coefficient of the other probes in solution, and for all probes in the lamellipodium (Figure 4C).

The probes are introduced into cells by electroporation, and fragmentation is subsequently induced as above. The electroporation solutions for the different probes, empirically adjusted to yield similar intracellular probe concentrations (suitable for FCS), contain: (i) 0.7 μM Alexa Fluor 488; (ii) 3 μM Alexa Fluor 488-actin in G-buffer or (iii) 3.5 μM Alexa Fluor 488-phalloidin which is premixed with dNTPs (as above). Fragments are imaged by DIC and in confocal mode immediately prior to FCS measurements, and a spot near the leading edge is chosen for FCS analysis (Figure 4A). ~20-50 autocorrelation measurements, lasting 2 s each, are carried out as the fragment is moving forward (and hence the analysis spot is moving along a line from its initial position in front of the cell, toward the rear of the lamellipodium, roughly perpendicular to the leading edge). For successive analysis, only the autocorrelation curves of intensity traces exhibiting uniform fluctuations are taken into account and averaged together, and the correlation function is averaged over a total time of 10-15 s in each fragment. Since very low labeling is used in the FCS experiments we expect that essentially all labeled diffusing species, including actin monomers and oligomers, contain a single label. In particular, diffusible filaments will be labeled by at most a single phalloidin, which is not expected to have a large influence on their stability.

A challenging aspect of the FCS measurements in live fragments as compared to bulk measurements (or e.g., measurements in the cell body) is that lamellipodium is very thin (~0.2 μm) and so has to be precisely located in the focus of the laser beam to within few hundreds of nanometers (i.e., less than the axial width of the beam waist). This is hard to achieve in a microscopy system, especially with the fragments moving over large distances. Invariably, a significant fraction of fragments are imaged slightly out of focus. The effective sampling area in this case is larger than in the proper focal plane, leading to larger apparent diffusion times. These measurements might have led to an artificially inflated variability in the data. However, they can be dismissed based on the apparent molecular brightness: FCS correlation function at short timescales multiplied by the average photon count rate gives the specific brightness of labeled molecules. This quantity is very sensitive to the overall alignment of the optical system, and, in particular, to the location of the measurement plane. Indeed, in all of our measurements which exhibit low molecular brightnesses we observe increased apparent diffusion times (as well as an increased spread in the diffusion times). We dismiss such data and keep only measurements with high molecular brightnesses for which there is no obvious correlation between these two quantities. Typically this means dismissing more than half of the data (those with the lowest brightnesses).

The correlation functions measured in fragments are fit with a model assuming simple 2D diffusion, since the height of the lamellipodium is much smaller that the axial beam waist (~2 μm) so the diffusion in the third dimension is irrelevant. Explicitly, we determine the best fit for the correlation function to: $G_{norm}(t) = g_0/1 + t/\tau_D$, where g_0, τ_D are taken as fit parameters. The fit range is taken as 0.1-100 ms for actin and phalloidin, and 0.01-100 ms for the free dye. Since diffusion times of phalloidin and actin are in the millisecond timescale, there was no need to account for triplet dynamics (which is in the few μs timescales). We used the simplest possible model since it is characterized by a single parameter – diffusion time - which can be compared consistently between different measurements, while giving reasonably good fits in the relevant range of timescales (Figure S3). The effective diffusion coefficient is directly determined from the diffusion time as, $D = w_{x-y}^2/4\tau_D$, where $w_{x-y} = 0.29\mu m$ is the determined beam waist radius.

To measure the relative abundance of diffusing oligomers relative to the total amount of filaments we use the amplitude of the Alexa Fluor 488-phalloidin FCS signal. During the FCS measurements we continuously illuminate a spot within the lamellipodium, which is fixed in the lab frame (and hence moves away from the leading edge in the cell frame of reference). As the network is stationary in the lab frame of reference, the network signal bleaches within a short distance from the leading edge, after which essentially all the measured counts emanate from diffusing filaments. Thus, the average FCS count rate in the lamellipodium is proportional to the amount of labeled diffusing filaments. However, since the labeling efficiency varies considerably between fragments (due to the variable amount of labeled probe introduced by electroporation), we need to calibrate the labeling efficiency for each fragment individually to deduce the fraction of diffusible filaments. This is done by imaging the same fragment in scanning confocal mode immediately before the FCS measurements (using the same illumination setting used for FCS) and determining the total fluorescent signal in the lamellipodium. The average background-subtracted pixel intensity in the lamellipodium will be proportional to the total amount of phalloidin. To compare the pixel intensities to the FCS count rate, we determined the (instrument-dependent) calibration factor, relating the pixel intensity in an image to the measured FCS count rate, by measuring both signals on a calibration sample containing Alexa Fluor 488 in solution.

To obtain the fraction of diffusing filament, we determine the ratio between the average FCS count rate and the average lamellipodial fluorescent signal in individual fragments. The FCS count is proportional to the diffusible phalloidin fraction, whereas the total fluorescence in the lamellipodium is proportional to the entire phalloidin pool (both network-bound phalloidin and diffusible phalloidin). The fraction of mobile filaments is thus determined as: (average FCS counts in the lamellipodium) / (average background-subtracted pixel intensity in the lamellipodium) * (calibration factor).

Estimate of oligomer size from FCS results

The oligomer shape can be approximated well as by oblate ellipsoid with one of the half-axis equal to the effective radius of an actin filament, r = 3.5 nm [48], and the other half-axis equal to the half-length of the oligomer, $l/2$. According to low Reynolds numbers' hydrodynamics, the formula that gives the ratio of the viscous drag of lengthwise movement of such an ellipsoid to that of a sphere of radius r, has the form $f_l = l/3r/\ln(l/r) - 0.5$, and similarly for the sidewise movement, $f_s = 2l/3r/\ln(l/r) + 0.5$ [49]. Note that these formulae describe the drag of an oligomer in the limit $r << l$. This is the relevant limit in our case, as the estimate below shows. The effective diffusion coefficient for an oligomer is equal to, $D_o = (D_{\parallel} + 2D_{\perp}/3) = (D(1/f_l) + (2/f_s)/3)$, where D is the diffusion coefficient of a sphere of radius r [50]. The effective radius of an actin monomer is $\tilde{r}$ ~2.5 nm, so the diffusion coefficient of a monomer is $r/\tilde{r}$ ~1.4 times higher than that of a sphere of radius r. Thus, the ratio of monomer to oligomer diffusion coefficients is equal to: $(1.4 \times 3 f_l f_s / 2 f_l + f_s)$. According to our measurements (Figure 4C), this ratio is equal to ~3, and so, $(1.4 f_l f_s / 2 f_l + f_s) \approx 1$, where $f_l = (l/3r/\ln(l/r) - 0.5), f_s = (2l/3r/\ln(l/r) + 0.5)$. We solve these algebraic equations and find, $l \approx$ 35nm. Note that this estimate is close to the mesh size of the actin network, ~50 nm [3], and so the sidewise movement of oligomers would be partially hindered and oligomer would move easier by reptation, lengthwise through the cytoskeletal pores. Therefore, we likely overestimate the oligomer length, but not significantly.

Quantitative image analysis

Image analysis is done using the celltool package developed by Zachary Pincus [51] and custom written code in MATLAB [31]. Fragment morphology is measured by representing fragment shapes as polygonal outlines. Briefly, fragment shapes are manually determined by using the ''magnetic lasso'' tool in Adobe Photoshop to trace the edge of each fragment, based on phase-contrast

images. Outlines are extracted from the masks to derive a series of (x,y) points corresponding to the fragment boundary. Each series is resampled to 200 points, evenly spaced along the boundary. Finally, the outlines are mutually aligned to bring the shapes into a common reference frame. The distributions for different probes along a cross section perpendicular to the leading edge are measured in individual fragments by averaging over 10 contour points (out of 200 contour points) around the center of the leading edge, along the cross section. Cross sections are plotted as a function of the normalized distance from the leading edge, along the front-to-rear axis (front-to-rear distance = 1).

Modeling

Mathematical predictions from simple conceptual models of actin transport

The initial hypothesis regarding actin turnover in motile cells was simple [52]: long actin filaments were assumed to span the lamellipodium and treadmill, with their barbed ends growing at the leading edge and their pointed ends shortening at the very rear (Figure S1Bi). Diffusion was thought to be responsible for recycling actin monomers from the rear to the front. In this model, transport of actin both in the network and as monomers is global: the network flows rearward (in the framework of the moving cell) across the entire cell before turning over, while monomers released at the rear diffuse across the whole cell before reassembling into the network at the leading edge. Straightforward analysis (below) shows that this model is inconsistent with experimental data, and instead brings forward two possible limiting scenarios: the network treadmilling model [8–10], in which actin assembly occurs primarily at the leading edge with slow network disassembly everywhere (global network turnover; Figure S1Bii), and the nucleation-release model [11, 12], where rapid actin assembly and disassembly take place throughout the lamellipodium (local network turnover; Figure S1Biii).

Let us investigate the simplified equation for actin network turnover and transport: $(\partial F/\partial t) = -V(\partial F/\partial x) - rF + aF$.

In this equation, we do not consider the details of network assembly, and simply lump them into an effective constant assembly rate a, which makes this equation self-consistent. The equation is complemented by a boundary condition for the network density. At the leading edge, we take the network density to be a constant $F(0) = F_0$. At the rear $(x = L)$, we assume that all the filaments that flow into the boundary convert into monomers and oligomers. The stationary solution of this equation is then: $F = F_0 \exp[-((r-a)x/V)]$.

In the filament treadmilling model, there is no turnover of the network throughout the lamellipodium, so $r = a = 0$. In this case the actin network concentration should be constant across the cell, $F = F_0$, while the monomer concentration would have a steep gradient, decreasing from rear to front, facilitating a diffusive flux of monomers toward the leading edge. However, observations in cells show that the lamellipodial actin network density decreases away from the leading edge [12, 31, 45], indicating that there is net actin network disassembly throughout the lamellipodium. Thus, any feasible model of lamellipodial actin turnover has to incorporate a slow net rate of actin disassembly everywhere, whereas models assuming that network disassembly is confined to the rear boundary (e.g., [52]) are inconsistent with the data.

The identification of the branching activity of Arp2/3 and the establishment of the dendritic nucleation model [8], led to the network treadmilling model (Figure S1Bii) [9, 10] which suggested that Arp2/3 mediated assembly of short branching filaments occurs near the leading edge, while gradual actin network disassembly takes place throughout the lamellipodium. In this model, actin turnover is global, as assembly occurs primarily at the leading edge and monomers have to travel across the cell from their disassembly site to the front. This scenario is supported by FRAP measurements in melanoma cells by Lai et al. [16]. In the simplest version of the network treadmilling model, there is only disassembly, but no assembly, throughout the lamellipodium, so $a = 0, r_{at} \neq 0$, and $F = F_0 \exp[-(r_{at}x/V)]$. Thus, in this model, the predicted network actin density decreases exponentially away from the front.

However, measurements of photoactivated actin in motile keratocytes showed that the network turns over much faster than the time over which the cell moves one body length [13]. These results prompted the nucleation-release model, which posited that short actin filaments appear, elongate and disassemble rapidly throughout the lamellipodium (Figure S1Biii). This model, in which actin network turnover is local, with rapid cycles of assembly and disassembly throughout the lamellipodium, is further supported by single molecule fluorescence speckle microscopy measurements in fibroblasts [12], and by a number of recent studies in neutrophil-like cells [14] and neuroblastoma cells [15]. In the nucleation-release model, there is rapid assembly and disassembly, nearly balancing each other, throughout the lamellipodium: $r_{nr} > a_{nr} > 0, r_{nr} - a_{nr} << r_{nr}$. The predicted network actin density also decreases exponentially away from the front, $F = F_0 \exp[-((r_{nr} - a_{nr})x/V)]$, and if $r_{at} = r_{nr} - a_{nr}$ then the network actin density is exactly the same as in the network treadmilling model. Thus, to distinguish between these two models, at least one rate, either r or a, has to be measured, in addition to observations of the actin network density profile.

To sustain a steadily moving front, cells have to maintain a sufficient concentration of monomers near the leading edge. Moreover, when cells initiate motility in response to chemical cues, they are able to recruit monomers to assemble a new leading edge within seconds [53]. These requirements set stringent demands on the efficiency of actin transport and turnover. Simple estimates show that if actin network assembly is confined to the leading edge, diffusion is fast enough for recycling monomers back to the leading edge [54]. However, if the network turns over locally, so that actin monomers can reassemble into the network everywhere, the effective diffusion-based monomer transport rate could slow down considerably, making diffusive transport insufficient to account for observed cell speeds and response times.

Fit for the barbed ends' distribution

We take the measured distributions of the uncapped barbed ends in a population of fragments (Figure 2; Figure S5B; N = 137), and average the measurements over the population as follows. We define, $B(x) = (1/N)\sum_{j=1}^{N} B_j(x)$, where $B_j(x)$ is the measured distribution in the j^{th} fragment as a function of the relative distance to the leading edge (assuming front-to-rear distance, L = 10μm). We

normalize the result, defining, $b(x) = (B(x)/\int_0^L B(x)dx)$. Then, we fit this averaged distribution to a function of the form, $b(x) = \lambda_1 + \lambda_2 \exp(-x/\lambda_3)$. The best fit is the function:

$$b(x) \approx 0.6 + 1.6 \times \exp(-x/3.3) \quad \text{(Equation 1)}$$

where $\lambda_1 = 0.6$ and $\lambda_2 = 1.6$ are non-dimensional, while $\lambda_3 = 3.3$ μm and x are measured in μm (Figure S5B).

The influence of membrane tension on protrusion

The membrane tension at the leading edge of motile fragments is $T \sim 300$ pN/μm [55]. We estimate the number of filaments abutting the membrane at the leading edge, based on the filament labeling experiments (Figures 1A–1C), to be $N \sim 400$/μm. Thus, the load force per filament is $f = 2T/N \sim 1.5$ pN. Both theoretical estimates [45], and experimental measurements [56], suggest that this force is well below the stall force for a pushing filament. Furthermore, application of a load force at the leading edge [57] and indirect measurements reported in [45], suggest that this force does not slow polymerization at the leading edge dramatically. We use the polymerization ratchet formula, $V \approx \delta k_{on} g \Phi, \Phi = e^{-f\delta/k_B T}$ [54], and the estimated load force per filament, to estimate the influence of load on the speed of protrusion. The mechanical factor, Φ, responsible for slowing down protrusion due to load, is less than 1, but not much less: if $f =$ 1.5 pN, $\Phi = e^{-f\delta/k_B T} = \exp(-1.5 \times 2.7/4) \approx 0.4$. In the calculations, we use the value $\Phi = 0.5$.

Model of actin turnover, boundary conditions and numerical methods

We first consider the average bulk concentrations of polymerizable monomers (g), non-polymerizable monomers (G), oligomers (short diffusing filaments which are disconnected from the network, f), and network actin (F). We assume that network actin disassembles into oligomers, and then oligomers disassemble into monomers, which in turn can switch between a polymerizable and a non-polymerizable form (Figure 5A). The average bulk concentrations for the four actin subpopulations (F, f, G, g) can be determined based on our experimental results and the assumption that the assembly rate of polymerizable monomers in vivo is similar to the measured rates in vitro. Importantly, since we know the amount of filamentous actin in absolute numbers (Figures 1A–1C), we can infer all the actual actin concentrations, giving: $F \approx 800$ μM, $f \approx 400$ μM, $G \approx 1200$ μM, and $g \approx 20$ μM (Figure 5A).

To specify the model, we need five effective reaction rates: network disassembly rate r, oligomer's disassembly rate c, monomer assembly rate a, and the rates of transition between the polymerizable and non-polymerizable monomers, β and k (Figure 5A). We directly measure only one of these rates, $r \approx 0.25$/s (Figure 3), but can infer the other rates from flux balance analysis (Figure 5A). At steady state, the number of actin subunits per unit time transitioning from the network into oligomers, rF, has to be equal to the number of subunits flowing from oligomers to monomers, cf, as well as to the number of monomers assembling back into the network, ag. Thus, $rF = cf = ag$, so that, $c = rF/f \approx 2r \approx 0.5$/s, and $a = rF/g \approx 40r \approx 10$/s. The parameter a can also be estimated independently from the in vitro actin polymerization rate, k_{on}, and the measured density of uncapped barbed ends (see below). This estimate agrees well with the value obtained based on flux balance analysis, providing a consistency check for the model.

The transition rates between polymerizable and non-polymerizable monomers, should similarly be related at steady state by a flux balance relation: $\beta g = kG$ (Figure 5A). To specify these transition rates separately, we introduce a second model assumption that the rate of actin-thymosin dissociation (which is assumed to mediate the transition of an actin subunit from the non-polymerizable monomer pool to the polymerizable one) is the same as that measured in vitro, so that $k \approx 2$/s [43, 44]. In this case, $\beta = kG/g \approx 120$/s. Note that this rate can also be independently assessed by multiplying the in vitro rate of actin-thymosin association, $\sim 1/\mu M \times s$ [4, 44] by the thymosin concentration which is estimated to be hundreds of μMs, giving the same order of magnitude value, again demonstrating the model's consistency.

After specifying the rate constants for the different actin reactions, we can study the spatial dependence of the model in the cell frame of reference explicitly, by incorporating rearward drift of the actin network (V) and diffusion of oligomers (D_f) and monomers (D). We use a 1D model to describe actin densities along the anterior-posterior direction (Figure 5B), since our microscopy data and numerous published results [3, 31, 45] indicate that changes in actin densities occur primarily along the front-to-rear axis, with little variation in the lateral direction (except for the very sides). Furthermore, the thickness of the lamellipodium in the dorsal-ventral direction is so small, that diffusion would equalize all diffusible actin densities along this axis, while the spatial distribution of the network on such small scale does not affect turnover and transport dynamics. Our model is thus described by a set of 1D reaction-diffusion-drift equations for the four actin subpopulations (in the cell frame of reference; Figure 5B). The three additional transport parameters for this model are all measured experimentally. Specifically, the rearward drift of the actin network (which is equal to cell speed) is $V \approx 0.2 \mu m^2$/s [31], and the diffusion coefficients for monomers (both polymerizable and non-polymerizable) is $D \approx 15 \mu m^2$/s, and for oligomers, $D_f \approx 5 \mu m^2$/s (Figure 4C). Below we consider the influence of cytoplasmic fluid flow [58], and show that the observed flow rates have a negligible effect on transport compared to diffusion (Figure S5A).

The network assembly rate is expected to be proportional to the product of the local densities of the polymerizable monomers g and the uncapped barbed ends' b. For simplicity, we fit the measured uncapped barbed ends' distribution to an exponential function (Figure S5B), and use the fit as an input in our calculations (see Equation 1 above). The third, and last, assumption of the model is that the network disassembly rate is proportional to local actin network density. This is the simplest plausible model for network disassembly, in which network filaments disassemble at a constant rate r, and this rate is uniform across the fragment. Moreover, recent work shows that this assumption holds in the lamellipodium of HL60 and B16-F1 cells [14].

There are thus four model equations (Figure 5B):

$$\frac{\partial F}{\partial t} = -V\frac{\partial F}{\partial x} - rF + ab(x)g \quad \text{(Equation 2)}$$

$$\frac{\partial f}{\partial t} = D_f \frac{\partial^2 f}{\partial x^2} + rF - cf \quad \text{(Equation 3)}$$

$$\frac{\partial G}{\partial t} = D \frac{\partial^2 G}{\partial x^2} - kG + \beta g \quad \text{(Equation 4)}$$

$$\frac{\partial g}{\partial t} = D \frac{\partial^2 g}{\partial x^2} + cf + kG - \beta g - ab(x)g \quad \text{(Equation 5)}$$

where *b(x)* is given by Equation 1. Equation 2 is a first order PDE, with a drift term with a constant velocity directed to the right. Therefore, at the leading edge, $x = 0$, we use a boundary condition that: $F(0) = F_0$. In other words, we define the network actin density at the leading edge. We estimate the value of the parameter F_0 from our measurements in the following manner. The actin filament concentration at the leading edge is ~1.8 mM (Figure 1B). Considering that our analysis suggests that the oligomer concentration is nearly uniform and is on the order of 0.4 mM, we take $F_0 =$ 1.8-0.4 mM = 1.4 mM in the calculations. Note also that, as we show below, the reaction terms in the model equations are much faster than the transport terms, so the network actin density throughout the fragment can be approximated by the ratio of the source and sink terms: $F \sim ag/r$. From this expression we can estimate the network density, $F \sim ag/r \sim 10\ s^{-1} \times 20\mu M \times 4\ s \sim 0.8$ mM, which turns out to be of the same order of magnitude as the value taken for F_0. This is the reason we do not observe any singularity in the boundary layer near the leading edge (see below).

At the rear, numerically, we simply let the network actin accumulate at the grid point corresponding to $x = L$. The value of the network actin density at the rear stabilizes because of the constant disassembly. In order to smooth the actin distribution at the rear, we introduce a small diffusion term close to the rear; physically, this can be justified by the observation that at the rear, the actin network, weakened by disassembly, is collapsing and deforming significantly [27], and probably randomly. As a result, the numerical solution predicts a peak in the network actin density at the rear, which is indeed observed (Figure 1B).

We take no-flux boundary conditions for the parabolic equations for the oligomer and non-polymerizable actin monomer concentrations, both at the front and at the rear, as well as for the parabolic equation for the polymerizable actin monomer concentration at the rear (monomers and oligomers cannot escape or enter the fragment). Derivation of the complex boundary condition for the polymerizable actin monomer concentration at the front follows the balancing argument in [54]: the flux of the network actin from the leading edge toward the rear is equal to $F_0 V$. This flux is balanced by the diffusive flux of the polymerizable actin monomers into the leading edge $F_0 V = D(\partial g/\partial x)$. On the other hand, $V \approx k_{on}\delta g(0) \times \Phi$. Therefore, we use the boundary condition: $\partial g/\partial x\,|_{x=0} = (F_0 \Phi k_{on}\delta/D)g(0)$. At each computational step, we compute the fragment speed as, $V \approx k_{on}\delta g(0) \times \Phi$. Thus, there are five parameters needed to define the boundary condition and compute the velocity; two parameters, k_{on}, δ, are known from many studies, we measure the values of D and F_0, and estimate Φ (above).

We use the finite difference method to solve the model equations numerically. The forward-time-centered-space method is used for the parabolic PDEs (Equations 3, 4, and 5; the temporal and spatial steps are chosen so that the stability condition is satisfied), and the first order forward time – upwind scheme is used for the hyperbolic PDE (Equation 2), with Courant–Friedrichs–Lewy stability condition satisfied [59]. We checked the solution converges to the same, unique, asymptotically stable, stationary solution from any initial conditions. The m-file for simulating the actin distributions using MATLAB is appended (Methods S1).

Scaling and dimensional analysis of the model

We rescale the model equations to make them dimensionless, using the inverse disassembly rate, $T = 1/r$ as the timescale, and the half-fragment length, $X = L/2$ (with $L = 10$ μm) as the spatial scale. We choose the characteristic scales of the concentrations, $\overline{F}, \overline{f}, \overline{G}, \overline{g}$, using the following considerations. The scales for $\overline{F}, \overline{G}$ are of the same order of magnitude as that of the total amount of actin, $\overline{A} = \overline{F} + \overline{f} + \overline{G} + \overline{g}$ and so we choose $\overline{F} = \overline{A}, \overline{G} = \overline{A}$. We choose two other scales using the balances of the average concentrations (the balances of the reaction terms in the model equations): $r\overline{F} = c\overline{f}, k\overline{G} = \beta\overline{g}$. Thus, $\overline{f} = (r/c)\overline{A}, \overline{g} = (k/\beta)\overline{A}$. Using these scales, the model equations can be re-written as:

$$\frac{\partial F}{\partial t} = -\left(\frac{2V}{rL}\right)\frac{\partial F}{\partial x} - F + \left(\frac{ak}{r\beta}\right)b(x)g \quad \text{(Equation 6)}$$

$$\frac{\partial f}{\partial t} = \left(\frac{4D_f}{rL^2}\right)\frac{\partial^2 f}{\partial x^2} + \left(\frac{c}{r}\right)(F - f) \quad \text{(Equation 7)}$$

$$\frac{\partial G}{\partial t} = \left(\frac{4D}{rL^2}\right)\frac{\partial^2 G}{\partial x^2} - \left(\frac{k}{r}\right)(G - g) \quad \text{(Equation 8)}$$

$$\frac{\partial g}{\partial t}=\left(\frac{4D}{rL^2}\right)\frac{\partial^2 g}{\partial x^2}+\left(\frac{\beta}{r}\right)(G-g)+\left(\frac{\beta}{k}\right)\left(f-\left(\frac{ak}{r\beta}\right)b(x)g\right). \quad \text{(Equation 9)}$$

For notational simplicity, we keep the original notations for all concentrations, time and space variables, while in fact in Equations 6, 7, 8, and 9 the variables are $F/\overline{F}, f/\overline{f}, G/\overline{G}, g/\overline{g}, t/T, x/X$. The great utility of this scaling is that, first, it allows us to understand the behavior of the actin distribution in terms of a hierarchy of key timescales. Second, it allows us to investigate the monomer density at the very leading edge by perturbation analysis (see below). Third, using it we can find an approximate solution analytically. Finally, we use the scaling to investigate the model's sensitivity to the parameter values.

The model behavior is determined by the values of three non-dimensional transport parameters and five non-dimensional reaction parameters. The scaled network assembly rate is, $ak/r\beta \sim 1$. The flow of the actin network is slow relative to the rates of network assembly and disassembly: $2V/rL \sim 0.15$. Diffusion of monomers is relatively fast compared to the rates of network assembly and disassembly: $4D/rL^2 \sim 4$, and of the same order of magnitude as oligomer disassembly $(c/r \sim 2)$, but considerably slower than fast de-sequestration of the monomers $(k/r \sim 8)$, which in turn is much slower than very fast monomer assembly $(\beta/k \sim 60)$, which is still much slower than the super-fast sequestration of monomers $(\beta/r \sim 500)$. Diffusion of oligomers is comparable to the rates of network assembly and disassembly: $(4D_f/rL^2) \sim 0.8$.

One of the conclusions from this hierarchy of timescales is that on a very fast scale, ~0.01 s, the polymerizable and non-polymerizable monomer densities equilibrate, so the polymerizable monomer density becomes proportional to the non-polymerizable monomer density. For dimensional variables, we have the relation: $g=(k/\beta)G$. On the scale of ~1s, oligomer density becomes proportional to the network actin density, and on the scale of ten seconds, the actin network density becomes steady, and diffusion spreads the monomers across the fragment. Indeed, it is very useful to consider the total monomer density, $\tilde{G}=G+g$. Adding Equations 4 and 5, taking into account that on the fast timescale $cf=rF$ and using the same scale, $\overline{A}$, for variable $\tilde{G}$, we obtain the following equation:

$$\frac{\partial \tilde{G}}{\partial t}=\left(\frac{4D}{rL^2}\right)\frac{\partial^2 \tilde{G}}{\partial x^2}+\left(F-\left(\frac{ak}{r\beta}\right)b(x)\tilde{G}\right). \quad \text{(Equation 10)}$$

Equation 10 has profound implications: monomers as a whole diffuse much faster than they undergo assembly, so their density become essentially constant across the fragment. Using non-dimensional variables, $g=const, G=const, f=F=(ak/r\beta)b(x)g$ (with different constants for g and G). Using dimensional variables, and taking into account that, $\int_0^L b(x)dx=1$, we obtain,

$$G\approx\frac{\overline{A}}{1+\left(\frac{ak}{r\beta}\right)}, F\approx\frac{\overline{A}}{1+\left(\frac{r\beta}{ak}\right)}b(x), f\approx\frac{r}{c}\frac{\overline{A}}{1+\left(\frac{r\beta}{ak}\right)}b(x)g\approx\frac{k}{\beta}\frac{\overline{A}}{1+\left(\frac{ak}{r\beta}\right)}. \quad \text{(Equation 11)}$$

Equations 6, 7, 8, and 9 constitute a singular perturbation problem. The only non-trivial part of this problem is the behavior of the polymerizable monomer density near the leading edge. In principle, this density could sharply plunge down at the leading edge due to monomer consumption at the leading edge, leading to local monomer depletion there. To investigate this problem, we take Equation 9 and drop the term in the last bracket because it is negligible compared to the sequestration-desequestration reaction term: $(\partial g/\partial t)\approx(4D/rL^2)(\partial^2 g/\partial x^2)+(\beta/r)(G-g)$. Then, we introduce a new spatial variable in the boundary layer at the leading edge: $x=zy, z=2(\sqrt{D/\beta}/L) << 1$. In dimensional terms, the width of the boundary layer is $\sim\sqrt{D/\beta}\approx 0.35$ μm and is hence not experimentally observable. Using this rescaling, the stationary distribution of the polymerizable monomers is given by the equation: $(d^2g/dy^2)+(G-g)=0$. The non-dimensional rescaled boundary condition is: $\partial g/\partial y\,|_{y=0}=(F_0\Phi k_{on}\delta/\sqrt{D\beta})g(0)$. The parameter $(F_0\Phi k_{on}\delta/\sqrt{D\beta})\sim 1$, which implies that there is no significant depletion of monomers at the leading edge, and even in the boundary layer the polymerizable monomer density remains roughly constant.

Independent estimate of the network assembly rate a

There are ~400 μm of filaments per μm^2 in the lamellipodium (Figure 1C). Considering that each filament in the lamellipodium is a few tenths of a micron long (supported by multiple studies, reviewed in [1]), there are ~1000 filaments per μm^2 in the lamellipodium. Assuming that a non-negligible fraction of them are uncapped, we estimate the area density of uncapped barbed ends in the lamellipodium to be on the order of, B ~100 ends per μm^2. Then, $\sim k_{on}Bg$ monomers per second are assembling per μm^2 in the lamellipodium. A concentration of 1 μM corresponds to ~100 molecules per 1 μm^2 in the lamellipodium (assuming a lamellipodial height of h = 0.2μm [3]), so the assembly rate in the lamellipodium will be $\sim k_{on}Bg/\eta$ μM monomers per second per μm^2, where $\eta \sim 100/(\mu M \times \mu m^2)$. This estimate should be equal to the assembly term, abg, in the model equations. The variable b is non-dimensional and is normalized to 1, so the estimate for the dimensional parameter is: $a \sim k_{on}B/\eta \sim$ (10/μM × s) × (100/μm^2)/(100/μM × μm^2) ~10/s, which is the same number we obtain from the flux balance analysis (Figure 5A). Note, that the exact value of the critical actin concentration, the value of which is well-known in vitro but can vary a few-fold in vivo due to the presence of various actin binding proteins, does not significantly affect the model's results.

Another consistency check is the following balance: Growing barbed ends at the leading edge extend the lamellipodium by ~1 μm in ~5 s (since V~0.2 μm/s), and so per micron of leading edge, one square micron of the actin network is assembled in ~5 s. In the middle of the lamellipodium, there are about two-fold fewer growing barbed ends and almost the same polymerizable monomer concentration as at the leading edge. Thus, considering that the network density is roughly two-fold lower in the middle compared to the

leading edge, the growth of these barbed ends has to rebuild the average network density in ~5 s. Therefore, the disassembly rate has to be ~1/(5 s), as observed (Figure 3).

Finally, note that keratocyte are one of the fastest moving cells so it likely that the concentration of actin and associated protein is higher in keratocytes than in other cell types. Moreover, fragments are pieces of lamellipodium that tore away from the main cell and the actin concentration tends to be enriched in the lamellipodium, so we expect the bulk concentrations of actin in fragments to be somewhat higher than in whole keratocytes, Thus, the bulk actin density we measure is high, but of the same order of magnitude, compared with measurements of the actin concentration in the lamellipodia of other cell types [3, 17], which is entirely feasible.

Cytoplasmic fluid flow has a negligible effect on transport

The easiest way to understand the relative effects of diffusion and cytoplasmic flow on the distribution of diffusible actin is to consider the diffusion-drift equation without the reaction terms with no-flux boundary conditions: $(\partial G/\partial t) = D(\partial^2 G/\partial x^2) - V_f(\partial G/\partial x)$, where V_f ~0.05 μm/s is the cytoplasmic flow in fragments (Figure S5A). The stationary solution of this equation is $G \propto \exp[V_f x/D]$, and so the ratio of the concentrations of diffusing actin at the rear to that at the front is, $\exp[V_f L/D]$, where L ~10 μm is the fragment's length. For monomers, $D \approx 15\mu m^2/s$, so, $\exp[V_f L/D] \approx 1.03$; for oligomers, $D \approx 5\mu m^2/s$, so $\exp[V_f L/D] \approx 1.1$. Thus, the effect of the measured flow on the monomer distribution is of the order of 3% relative to that of diffusion and is completely negligible. Similarly, the effect on the oligomer distribution is 10%, which is still relatively small. Numerical computations show that inclusion of the reaction terms does not increase the negligible effect on the monomer distribution, and diminishes the effect on the oligomer distribution even further.

Another indication that fluid flow of this magnitude has little influence on actin turnover comes from comparing fragments and whole cells. The measured fluid flow in whole cells [58], is roughly of the same magnitude but is directed in an *opposite* way (because myosin-generated pressure is more prominent at the rear of cells compared to fragments and this pushes the fluid toward the leading edge in cells [58]). Despite this difference in the direction of fluid flow in the lamellipodium (rearward in fragments versus forward in whole cells), the actin dynamics in cells and in fragments are essentially the same.

Balance of the diffusive and drift fluxes

We checked numerically that for the stationary numerical solution of the model equations reported in the main text (Figure 6A), the total actin flux, $J = VF - D_f(df/dx) - D(d(G+g)/dx)$, is equal to zero everywhere with high accuracy, as expected at steady state. Thus the network actin flux rearward is exactly balance by the diffusive flux of actin monomers and oligomers. It is easy to estimate the expected monomer concentration gradient. First, we can omit the effect of oligomers, because they diffuse slower than monomers, their concentration is much smaller than that of monomers, and their spatial concentration gradient is of the same order of magnitude as that of monomers. Thus, $VF \approx D(d(G+g)/dx) \sim D(\Delta(G+g)/L)$, where L ~10 μm is the fragment length, and $\Delta(G+g)$ is the difference in monomer concentrations between front and rear. Therefore, $\Delta(G+g) \sim (VL/D)\langle F\rangle$, where $\langle F\rangle$ is the average network actin concentration. According to our measurements, $\langle G+g\rangle \approx 1.5\langle F\rangle$, and so $(\Delta(G+g)/\langle G+g\rangle) \sim (2VL/3D)$ ~0.09. Thus, the difference in the monomer concentrations between front and rear is less than 10% of the average monomer concentration.

Note about the diffusion of monomers and oligomers in a fragment with variable height

Using the volume marker, we measured the height profile *h(x)* in fragments, which is not uniform. Rigorously speaking, for the diffusion part of the reaction-diffusion equations we have to write [54]: $(\partial g/\partial t) = D(\partial^2 g/\partial x^2) + (D/h)(\partial g/\partial x)(\partial h/\partial x) + R$, where R are the reaction terms. Namely, we have an additional term $(D/h)(\partial g/\partial x)(\partial h/\partial x)$ in the right hand side. However, the relative magnitude of this additional term compared to the main diffusion term, is on the order of $\Delta h/h$, where Δh is the standard deviation of the height *h(x)* of the fragment. The ratio $\Delta h/h$ is much less than 1, so this additional term introduces only small corrections. The same arguments apply to all other reaction-diffusion equations in the model, and a similar argument applies to the reaction-drift equations. Moreover, we solved the model equations including this term with a function *h(x)* corresponding to the measured height profile *h(x)* of fragments, and found very little difference from the fixed-height model predictions.

Model robustness and sensitivity to parameter values

Our model provides a coarse-grained picture of lamellipodial actin turnover. We do not consider explicitly the many detailed molecular processes involved in actin dynamics in vivo, including but not limited to ATP hydrolysis [1], accelerated actin assembly by profilin [60], stochastic effects [61, 62], the influence of the complex molecular 'polarizosome' machinery at the leading edge [63], and many other complex and synergistic actions regulating the dynamics, topology and structure of actin networks [7, 64]. Incorporating all these details into a model is not yet possible since the biochemical details are still unfolding, and many of the rates required to calibrate such a model are currently unknown. Importantly, however, we find that our model and its conclusions are extremely robust.

The data show that the fragments' lengths vary about two-fold; these variations do not affect the model predictions significantly. There are three transport parameters in the model: the fragment speed V and two diffusion coefficients (D, D_f). Few-fold variations in any of these parameters do not change the model predictions. Greater variations in the length and the transport parameters are very unlikely. The uncapped barbed end distributions (function *b(x)*) exhibits substantial spatial variations between fragments. According to the model predictions, the network actin distribution is proportional to the uncapped barbed end distribution (because of the diffusion and transport effects, *F(x)* has a smoother profile than *b(x)*, plus the peak at the rear). Thus, variations in the function *b(x)* cause proportional variations in the function *F(x)*, which is in fact observed (Figures 6C–6E).

We vary the rate of oligomer disassembly, *c,* by an order of magnitude, and expectedly, find that this proportionally changes the average oligomer concentration, but the respective spatial distribution of oligomers and all the other actin species do not change. The rate of actin network disassembly, *r,* cannot be much faster than observed (Figure 3): it takes a filament an order of one second to

grow before getting capped, and it is unlikely that individual filaments are stable for less than a few seconds. Decreasing the value of this parameter by up to a few-fold does not change any of the model results qualitatively.

The rate of monomer assembly *a*, can in principle vary significantly, as its value is estimated from in vitro data. The monomer assembly rate in vivo cannot be much higher than the measured in vitro rate, because monomer assembly is diffusion limited [1]. Of course, there are effects of thymosin (thymosin-bound monomers were shown to be specifically used for formin-mediated elongation at the leading edge [15]) and profilin (that steers polymerization to formin-bound barbed ends). The model, however, shows that a limited, few-fold, increase of the monomer assembly rate does not change the results qualitatively. It is very probable that the respective in vivo assembly rate is slower, even by an order of magnitude. Remarkably, significant slowing down of the assembly only improves the model's qualitative behavior (monomer recycling being global and monomer density being constant). Indeed, a lesser rate of monomer assembly would keep the monomers in the cytoplasm longer. The only change in this case, according to the model, is an increase in the average polymerizable monomer concentration, which would be inversely proportional to *a*. If *a* decreases by an order of magnitude, *g* increases to ~200 μM, which is still much less than the predicted non-polymerizable monomer concentration.

The rates *k* and β are also estimated based on in vitro data, and thus could vary by an order of magnitude in vivo. For the model's predictions to remain qualitatively unchanged, two strong inequalities have to hold: $\beta >> a$, $\beta >> k$. These conditions ensure that the non polymerizable actin pool is large and exchanges rapidly. Variations in these parameters simply change average concentrations of the monomer species, but do not affect any crucial temporal or spatial scales. The second of these inequalities is extremely robust, because we estimate the value of β to be greater than that of *k* by two orders of magnitude. The rate *a* is very unlikely to be faster than that in vitro, and so the rate β can vary at least by a few-fold without affecting the model's behavior.

Of course, if all the parameter values are changed at once by a few-fold, our conclusion about the global character of monomer recycling and the uniformity of the monomer distribution could be violated. However, the scaling analysis allows the following simple conclusions: if four inequalities, $(D/rL^2) \geq 1$, $\beta > > a, r, k$, are valid, then so are all qualitative model predictions. Regardless of the molecular details involved, this ensures that the diffusible actin monomer transport is global and that the monomer density is insensitive to spatiotemporal fluctuations.

Other possible actin reaction networks

We did not consider explicitly many known reactions (the complete list of these reactions can be gleaned from [54]). In addition, the assumed core topology of the reaction network could be somewhat different. Here we consider five modifications to the actin reaction network (Figure S4), and argue that these changes do not affect the principal conclusions of the model. First, we add profilin and a respective few fold acceleration of the monomer assembly reactions (arrows marked '1', Figure S4). Mathematically, this would mean the addition of an equation for the concentration of G-actin-profilin, which would be relatively trivial. We tested the results for known concentrations of profilin and reaction rates [54, 65], and did not find any nontrivial changes in the model predictions. If the rate of elongation is faster due to the presence of formins, the estimate of the polymerizable actin monomer concentration needed to explain the observed actin polymerization rate would be even lower, making our main point that most of the diffusible actin is not potent for polymerization even more dramatic.

Similarly, it is relatively trivial to add G-actin-cofilin and respective reactions to the model (arrows marked '2′, Figure S4). Again, the addition of such a term, for known concentrations of cofilin and reaction rates [54, 65], does not lead to any nontrivial changes in the model predictions. Similarly, reactions with a number of other actin binding proteins could be added, but this only makes the model more cumbersome without changing its qualitatively interesting features.

Assembly of monomers onto the ends of oligomers (arrow marked '3′, Figure S4) is also a plausible possibility. We tested this, and as far as the rate of monomer assembly onto oligomers does not exceed the rate of oligomer disassembly, the results do not change. As discussed in the main text, the oligomers can also slowly reassemble into the actin network (arrow marked '4', Figure S4). This process is, in general, unlikely, and at most it is much slower than monomer assembly. Mathematical tests show the model's predictions do not change if slow oligomer reassembly is included.

One intriguing possibility is that some of the non-polymerizable actin pool is in the form of actin dimers or trimers which diffuse nearly as fast as monomers. If these actin multimers appear from breaking of larger oligomers, and if their assembly into the network can be neglected, then a reaction shown in Figure S4 with an arrow marked '5′ has to be introduced. We find that adding this reaction does not change the model's predictions about the nature of network turnover and monomer recycling. The only change in this case is that density *g(x)* is no longer uniform, and starts to depend on the local actin network density.

The model, of course, does not contain the molecular details of disassembly, including hydrolysis, Arp2/3 being dissociated from pointed ends, the effect of various cofactors, etc. Adding these details, and especially, nucleotide-specific assembly and disassembly rates could introduce a non-uniform distribution of the actin network disassembly rate, which again would not change the model's predictions, other than introducing deviations from the network density being exactly proportional to the uncapped barbed end density.

Dynamics of lamellipodial actin turnover and their implications for motility

To understand the implications of having a vast non-polymerizable diffusible actin pool (containing both oligomers and non-polymerizable monomers), we perform numerical experiments simulating the system's response to various changes in actin network dynamics in space and time (Figure S6). We compare four different scenarios (Figure S6A); in the first scenario we consider the model described above, in which the concentration of non-polymerizable monomers (*G*), and oligomers (*f*) is large (*G, f >> g*; β = 120/s, *c* = 0.5/s). For comparison, we consider other scenarios in which we modify the monomer sequestration rate (β) and the oligomer disassembly rate (*c*), to make the pool of non-polymerizable monomers and/or oligomers much smaller. Specifically, in the second

scenario, we assume the rate of monomer sequestration β is equal to the monomer de-sequestration rate k (i.e., β = 2/s), so G is substantially reduced, $G \approx g$. All other reaction rates and concentrations (f, g, F) are assumed to be the same. In the third scenario, we also substantially increase the oligomer disassembly rate, taking c = 50/s. The oligomer concentration becomes negligible, because oligomers disassemble very fast. Thus, in this scenario we have $G \approx g$ and $f \approx 0$. In the fourth scenario, we essentially eliminate the non-polymerizable diffusible actin pool entirely, by taking β = 0.02/s and c = 50/s, so that, $G \approx f \approx 0$.

First, we examine the stability of the polymerizable monomer concentration at the leading edge (and hence the stability of cell speed). We introduce temporal fluctuations to the model by varying the network assembly rate at front of the cell periodically over time. Specifically, we vary both the parameter F_0 (the boundary condition for network density at the leading edge) and the amplitude of the function $b(x)$ (describing the density of uncapped barbed ends). From our experimental observations, we assess the typical amplitude for actin network density fluctuations to be tens of percent (Figure 1), over typical timescale of tens of seconds (e.g., as shown in Ofer et al. [31]). Thus, in our numerical experiment, we choose to vary the network density by 30% (both F_0, and the amplitude of $b(x)$) with a time period of 20 s (Figure S6B). The computed polymerizable monomer concentration at the leading edge fluctuates little (Figure S6Bi). This is easy to understand: the rapid exchange with the vast non-polymerizable, diffusible monomer pool buffers fluctuations. In contrast, without the large non-polymerizable actin pool, the polymerizable monomer concentration exhibits substantial fluctuations (Figures S6Bii–S6Biv), which would translate to large variations in speed over time.

Second, we consider the time it takes the system to respond to an abrupt change in actin dynamics (Figure S6C). There is evidence that cofilin activation is involved in the process of motility initiation after chemotactic activation [66], so we analyze how a sudden local increase in network disassembly influences actin dynamics across the cell. To that end, we examine the effect of an abrupt increase in network disassembly at the trailing end, on the polymerizable monomer concentration (and hence cell speed) at the leading edge. We find that released monomers reach the opposite edge of the cell within seconds, so that the monomer concentration rises to a new steady state level at the front within seconds (Figure S6Ci). Thus, a local increase in disassembly, anywhere in the cell, makes it possible for a cell to assemble a new leading edge within seconds.

Interestingly, when the non-polymerizable actin monomer pool is small ($G \approx g$), it still takes just a few seconds for the polymerizable monomer concentration at the leading edge to increase (Figure 6Cii). It turns out that this is due to the relatively rapid diffusion of oligomers, which can also contribute to transport of disassembled actin to the leading edge. Indeed, it takes $\sim 1/c \approx 2$ s for oligomers to disassemble into monomers according to the model, and during this time, according to the measured oligomer diffusion rate (Figure 4C), oligomers diffuse over distances of the order of ∼5μm, which is equal to half the lamellipodial width. To show that the oligomers are indeed responsible for rapid actin transport when the non-polymerizable actin pool is small, we simulate a scenario in which oligomers disassemble rapidly (c = 50/s), so the steady state oligomer concentration is close to zero (Figure S6Ciii). We find that after an abrupt increase in network disassembly at the rear, the polymerizable monomer concentration at the leading edge increases partially over just 1-2 s, but then continues to increase toward a new steady state over ∼20 s (Figure S6Ciii). It turns out that the initial rapid increase is due to the non-polymerizable actin monomer pool: even if this pool is small, it takes ∼0.5 s for the sequestered monomer to switch to the polymerizable form, and over this time, a monomer can diffuse ∼4 μm. Thus, half of the released monomers (the other half is polymerizable and reassembles immediately) can diffuse over large distances immediately after the abrupt increase in local disassembly. To confirm that in the absence of both oligomers and non-polymerizable actin monomers, the transport of actin becomes very slow, we simulate the model in a fourth scenario ($G \approx f \approx 0$). Indeed, we find that in this case, the effect of enhanced disassembly at one side of the cell, reaches the other side slowly, over ∼20 s (Figure S6Civ): monomers released from the network reassemble rapidly in the vicinity of their disassembly site, so they are able to reach the opposite cell edge only after many cycles of disassembly-diffusion-reassembly. The actin monomer transport thus becomes local, and it takes considerably longer for subunits to traverse across the cell. Thus, a large non-polymerizable actin monomer pool, or a large oligomer pool assisted by even a small non-polymerizable monomer pool, are sufficient for making actin monomer transport global, and facilitating a rapid (∼few seconds) response to internal or external cues. Yet, in the absence of all non polymerizable diffusible actin subpopulations ($G \approx f \approx 0$; scenario (iv)), actin monomer transport becomes local, and the system response to cues is much slower than the time it takes an actin monomer to diffuse across the cell.

Thus, we demonstrate that when actin disassembly rate fluctuates over time, fluctuations of the polymerizable actin are substantially suppressed due to the buffering effect of the large non-polymerizable pool (Figure S6B). Similarly, the large non-polymerizable actin pool will buffer spatial variations in actin dynamics (e.g., a local increase in the number of growing barbed ends), and hence suppress fluctuations in protrusion rates along the leading edge. On the other hand, if network disassembly is enhanced at one side of the cell, released actin subunits become available at the other side within seconds (Figure S6C). These predictions are in agreement with observations of chemotactically activated neutrophils which build a new leading edge within seconds [53], and experiments in breast cancer cells showing that actin from the cell body is incorporated at the leading edge within ∼10 s [15].

The model predicts that the polymerizable monomer distribution is proportional to the non-polymerizable monomer distribution to a high degree, due to the fast exchange between the polymerizable and non-polymerizable actin pool. This keeps the polymerizable monomer concentration near the leading edge essentially insensitive to local depletion by many growing barbed ends, as was predicted by earlier simplistic models [54, 67]. This feature of actin turnover makes cell speed robust, yet highly amenable to regulation, for example, by changing the concentration of actin sequestering proteins. To further understand actin turnover during non-steady migration, more detailed experiments and modeling will be needed.

Lastly, the proposed model makes it possible for a cell to rapidly increase the total amount of network actin if needed, without comprising the concentration of polymerizable monomers or cell speed. Such changes are observed experimentally in keratocytes

that are perturbed by abruptly increasing their membrane area by fusing giant liposomes [68], or in breast cancer cells that increase their area after stimulation [18]. Similarly, experiments in leukocytes showed that ~10-30 s after chemoattractant activation, both the actin network density and speed increase, while the total diffusible actin pool decreases [46]. In the model, this is achievable by simply decreasing a single parameter (β), basically, unloading some of the reserve non-polymerizable monomer pool into the network. This can be done by deactivating thymosin, for example. Without the large non-polymerizable actin pool, increasing the amount of network actin necessarily comes at the expense of decreasing the amount of polymerizable monomers, and hence would slow cells down.

Additional discussion of relevant pathways of actin turnover

Recent research shows that the molecular pathways of actin disassembly are complex, and involve the synergistic action of a host of actin-binding proteins, including coronin, cofilin, Aip1, twinfilin, and Srv2/CAP [22–25]. Similarly, actin assembly involves both Arp2/3 and/or formin and their relative importance and respective roles are still open questions in the field [69, 70]. It is also not possible currently to measure or infer the actin monomer concentrations available for assembly by either of these nucleators. Many additional biochemical details, such as the specific actin isoforms present, will influence the kinetics of nucleation and assembly. Moreover, the stability of filament nucleated by the different nucleators could be different (e.g., due to the effects of tropomyosins). Thus many biochemical details relating to actin assembly and disassembly dynamics in the lamellipodium are still not well-understood, certainly not in a quantitative manner.

Another issue to consider is the interaction and competition between different actin structures in the cell. Typically, several distinct actin structures coexist within a cell. While these structures can vary in their biochemical composition, many of their components, and in particular actin, are shared. This implies that the dynamics of the lamellipodial actin network are coupled to other cellular actin structures. While this is not relevant for fragments which are essentially stand-alone lamellipodia, most motile cells have additional prominent actin structures including the lamellum, the cortex and stress fibers (e.g., [15, 29]). There is evidence that the turnover rates differ significantly among these different actin substructures [15, 16, 71, 72], and that the actin exchange between them is complex, combining global and local recycling [15]. In addition, myosin contraction [27] and local tension on filaments [73] can contribute nontrivially to actin disassembly rates. The mechanisms for actin transport between different structures across the cell can also involve additional transport mechanism. In particular, diffusion can become insufficient for monomer transport in very long cells, or in cells that lack the vast non-polymerizable monomer pool. In such cells, directed actin transport, by fluid flow [38, 58] or motor-assisted transport, could become important for monomer transport. In principle, actin could also be synthesized *de-novo* locally near the leading edge by specific mRNAs delivered by microtubule-based molecular motor [74].

Trying to tease out all the details regarding actin assembly and disassembly in the lamellipodium is thus a formidable task, which is beyond the scope of our current manuscript. Our aim here is to provide a coarse overview of actin turnover in the lamellipodium, despite the lack of detailed understanding of actin assembly and disassembly dynamics in the lamellipodium. The limited current understanding of the microscopic details involved precludes the ability to describe the system with a truly microscopic model. Yet, the coarse grained picture we present is still useful and provides new insight, even though it cannot answer detailed mechanistic questions.

In the future, our conclusion of the globally distributed assembly in the lamellipodium will have to be reconciled with previous reports that photo-activated actin monomers seem to add mostly at the leading edge in live cells [15]. Aside from the obvious possibility that the actin dynamics are inherently different in the different cell types, we would like to note that the barbed ends labeling in extracted cells and the photo-activation experiments do not report exactly the same thing. Photo-activation experiments report on actin incorporation in live cells, which depends both on the availability of free barbed ends and on the local assembly rate which will determine how many actin monomers will be incorporated per free barbed end per unit time. The free barbed ends labeling experiments are done under uniform assembly conditions so every free barbed end is labeled with the same efficiency. There are many proteins that can modulate the actin assembly rate, e.g., formins. It is possible that the difference between our results on the spatial distribution of free barbed ends, and the patterns of actin incorporation in lamellipodia observed in the photo-activation experiments, are due to local variations in the actin assembly rates, rather than differences in the distribution of free barbed ends.

Difficulties of measuring monomeric actin concentrations directly

The pool of actin monomers in cells is composed of multiple subpopulations, which differ in their ATP/ADP state and in the variety of possible monomer binding partners (e.g., profilin, thymosin, cofilin). Importantly, the size and characteristics of the monomer pool available for polymerization in cells are unknown, and there are currently no direct ways to measure them. In vitro measurements of actin assembly rate, ~10/μM × s [43], indicate that ~10μM of actin monomers would assemble onto growing barbed ends at a rate of ~100 monomers per second. Given the nm-scale size of a monomer, this translates to a growth rate of ~0.1 – 0.3 μm/s, comparable to the speed of rapidly moving cells like keratocytes. Thus, if most of the diffusible actin (> 100 s μM) were available for assembly, the actin polymerization speed would be orders of magnitude higher than the fastest observed cell speeds, unless filament growth at the leading edge was considerably slowed down by an opposing force (e.g., due to membrane tension). Alternatively, the majority of actin monomers could be sequestered, e.g., by thymosin, making them unavailable for polymerization. In this scenario, the sequestering proteins would also need to be present at high concentrations, in the hundreds of μMs range [4]. The concentration of polymerizable actin in this scenario would be much lower than the total actin monomer concentration, but would still have to be high enough (at least ~10 μM) to support the observed polymerization rates. Another puzzle is how cells are able to maintain a monomer concentration which is considerably higher than the critical actin concentration which is even lower in the presence of profilin [4, 75]. The funneling hypothesis [76] proposed that many uncapped pointed ends in the cell are leaking monomers faster than in vitro

disassembly rates, with the help of cofilin and other cofactors, creating a higher concentration of actin monomers which facilitates rapid growth of fewer uncapped barbed filaments. However, the funneling hypothesis, was recently challenged [77]. To add to this complexity, there is also emerging evidence for the presence of several biochemically distinct pools of actin monomers assembling in a spatially segregated way to structurally different actin networks [15].

Direct measurements of the monomeric actin concentration in cells are notoriously difficult. Early use of fractionation of cell extracts and the DNase I inhibition assays gave widely distributed estimates for the diffusible actin concentration in cells, between 10 – 300 μM (reviewed in [4]). Subsequent experiments, comparing the intensity of actin fluorescence before and after extraction of the diffusible actin fraction in B16-F1 mouse melanoma cells [17], or using fluorescent decay after photoactivation in breast cancer cells [18], indicated that the concentration of actin monomer is in the range of hundreds of μMs. The photoactivation experiments were further used to show that the actin monomer concentration is roughly uniform across the cell [18]. The spatial distribution of actin monomers in cells was examined by staining cells with actin monomer binding probes, such as DNaseI and Vitamin D Binding Protein (VDBP). The staining intensity increased from front to rear in fibroblasts [19], but exhibited higher levels near the leading edge in nerve growth cones [20, 21]. It is unclear what subpopulation of actin is detected in these staining experiments since the probes' binding sites overlap with the some of the binding sites for actin binding proteins such as profilin, gelsolin and thymosin [78–81]. Note that the latter results, which suggest that the monomer concentration at the leading edge is higher than elsewhere, are not consistent with diffusive monomer transport to the leading edge, since diffusion can only drive monomers down a concentration gradient.

Open questions and relevance to other cell types

Our results show that the actin network in keratocyte fragments turns over locally, undergoing multiple cycles of disassembly-reassembly over the duration of the actin array treadmill. This seems to be a common feature of lamellipodial motility. Indeed, in keratocytes crawling slowly in cold temperatures, Theriot and Mitchison [13] found that the turnover time is 23 s, while it takes about 200 s for the actin array to treadmill from front to rear, at a speed of 0.05 μm/s across a ~10μm long lamellipodium, so there are ~10 cycles of reassembly across the lamellipodium. Similarly, in *Xenopus* fibroblasts, the turnover time is 30 s, while the treadmill duration is about 300 s (L/v ~8 μm / 0.025 μm /s) [12]. In fast-moving neutrophil-like cells, Lewalle et al. found that there are about 8 cycles of actin turnover as the lamellipodium moves one body length with speed similar to keratocytes [14]. Similarly, ~8 cycles of actin turnover per treadmill were found in the neuroblastoma cells' lamellipodia [15]. However, in other systems, the pattern is different: there are significantly fewer reassembly cycles in slow (~0.05 μm /s) mouse melanoma cells with very narrow lamellipodia (~2 μm), in which the treadmill duration is ~40 s, and the actin turnover time is between 13 and 37 s [16], so there are only 1-3 turnover cycles.

One of the central findings of this work is that actin monomer transport in lamellipodial fragments is global. The model predicts that the concentration of diffusible actin will be nearly constant in the cell, due to the large subpopulation of non-polymerizable monomers. Evidence from several other cell types suggests that this is a feature characterizing lamellipodial dynamics in other cells as well. For example Kiuchi et al. [18], showed that the diffusible actin concentration is roughly uniform across the cell in breast cancer cells. Furthermore, our model predicts that the leading edge protrusion should decrease if thymosin concentration is increased locally, since the local concentration of polymerizable monomers is expected to drop. This is exactly the observed effect of photo-activation of caged thymosin in motile keratocytes [82]. Recent studies in other cell types show that the recycling patterns can be more complicated [15, 83]. For example, studies in breast cancer cells show that actin monomers incorporating into the leading edge originate both from a global cytosolic pool and locally from recycled lamellipodial network actin, and that inhibiting thymosin hinders global, but not local, recycling [15]. Similarly, measurements in B-16 melanoma cells show that actin monomer transport across the lamellipodium is rapid, but suggests that the redistribution of actin subunits from the cell body into the lamellipodium can be delayed [83].

An important open question concerns the dynamic architecture of the actin network. Multiple observations provide clear evidence that the lamellipodial network behaves as a coherent, mechanically connected, structure. In particular, high resolution analysis of the lamellipodial actin network architecture by electron microscopy [84] show that the network is well-connected and that the filaments are mostly oriented with their barbed ends toward the leading edge. Furthermore, functional analysis of the mechanical integrity of the lamellipodium by direct application of forces on the cell body with a micropipette [85], as well as the coherence of the actin network flow field measured by fluorescence speckle microscopy [27, 29], both indicate that the network is mechanically well-connected. How does the lamellipodial network remain mechanically and structurally coherent if it turns over several times from front to rear?

While we cannot provide definitive answers to these intriguing questions, it is interesting to note that we consistently find a considerable fraction of the network actin (up to 1/3 ~10% unrecovered fraction / 30% network fraction) which does not recover after photobleaching (Figure 3C). These observations suggest that perhaps the network contains a subset of 'scaffolding' filaments that do not turn over as rapidly, and help keep the overall network architecture intact, as nascent filaments branch off existent filaments. What is the nature of these 'scaffolding' filaments? What could confer their enhanced stability? Currently there is no direct evidence for scaffolding' filaments, nor any knowledge of their molecular composition, but we can speculate about possible mechanisms. One possibility is that the filaments' stability is related to the type of nucleator that initiated them, as there is evidence for both Arp2/3 and formin-based nucleation in the lamellipodium. This is supported by recent results showing that the filaments generated by different nucleators have differential influence on protrusion dynamics and lamellipodial stability [69]. Stable filaments could also be defined by selective, cooperative association with actin binding proteins, such as tropomyosins [86] or coronin [16]. Yet another exciting possibility is that scaffolding filaments are stabilized by tension [73].

Another important question relates to the nature of the non-polymerizable actin monomer pool. Is thymosin-β4-governed sequestration the main factor that prevents monomers from polymerizing into the network? We do not have a good estimate for thymosin concentration in keratocytes; physiological range of thymosin concentrations in other cells, reviewed in [4], extend up to 500 μM, which is of the same order of magnitude, but still a few-fold less than what would be necessary for sequestering the ~1 mM of actin monomers we observe in keratocytes. Limited ADP/ATP exchange rates cannot account for the majority of sequestration, since the rate of ADP-actin assembly is high enough to deplete the monomer pool to ~0.1 mM, which is an order of magnitude less than measured. Moreover, direct analysis of the nucleotide-binding state of actin in *Xenopus* extracts showed that most of the actin monomers are ATP-bound [87]. It is not out of the question that in some cell types, different isoforms of actin, with much slower polymerization kinetics, coexist in the lamellipodium, but we do not think this is sufficient to explain the limited effective monomer assembly rates in keratocytes. To our minds, there are three intriguing possibilities other than thymosin that should be explored in the future. One is that there are multi-repeat β-thymosins that are capable of simultaneously binding more than one monomer [88]. Another is that monomers are actually the minority of the diffusible actin pool, and most of the actin is present as dimers and trimers that do not polymerize as efficiently. Oligomers were shown to be able to assemble into the network [89]. However, the relevant rates for assembly of oligomers of different sizes have not been accurately measured, even in vitro, so this hypothesis still has to be examined. Finally, estimates [65] suggest that up to a third of actin is transiently associated with the polymerization machinery (e.g., by being bound to Arp2/3, VASP, formin, etc) [90]. More careful analysis on partitioning of the total actin pool in the future will help resolve this important question.

QUANTIFICATION AND STATISTICAL ANALYSIS

The quantification of the data is detailed in the relevant sections above. No statistical analysis of the data was performed.

DATA AND SOFTWARE AVAILABILITY

The m-file for simulating the actin distributions based on the model equations (Equations 2, 3, 4, and 5) using MATLAB is appended (Methods S1).

Current Biology, Volume *27*

Supplemental Information

Actin Turnover in Lamellipodial Fragments

Dikla Raz-Ben Aroush, Noa Ofer, Enas Abu-Shah, Jun Allard, Oleg Krichevsky, Alex Mogilner, and Kinneret Keren

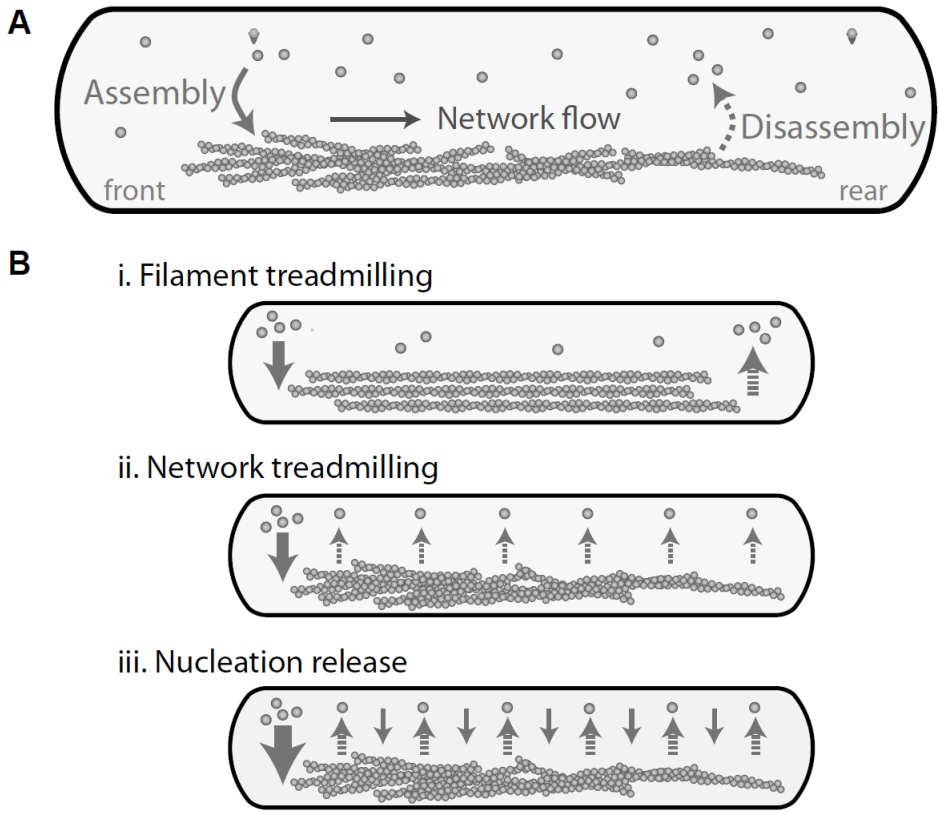

Figure S1. Models for actin turnover in lamellipodial motility, Related to STAR Methods. (A) Schematic illustration of actin turnover in a motile fragment. Polymerization of the lamellipodial actin network drives protrusion at the leading edge. As new actin assembles at the leading edge, the network is pushed rearward in the cell frame of reference and disassembles. Actin subunits dissociate from the network into the cytoplasm, and eventually reassemble into the network. (B) Different models for lamellipodial actin network turnover: (i) Filament treadmilling: filaments assemble by polymerization at their barbed ends at the leading edge, and disassemble from their pointed ends at the rear. (ii) Network treadmilling: the lamellipodial network assembles primarily by polymerization at barbed ends at the leading edge, and slowly disassembles throughout the lamellipodium. (iii) Nucleation release: lamellipodial protrusion is driven by polymerization at the leading edge, but network turnover is local, with assembly and disassembly occurring throughout the lamellipodium.

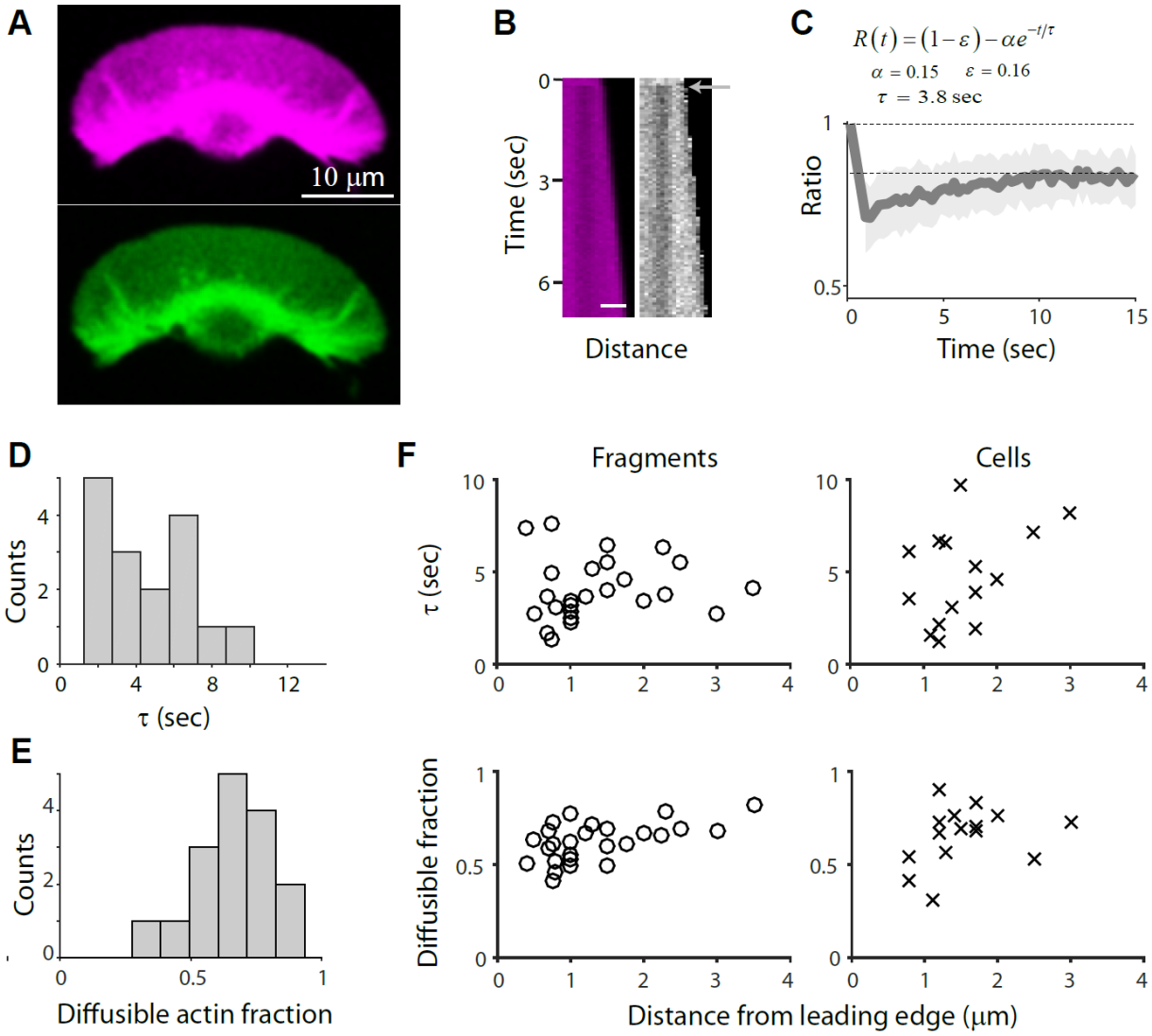

Figure S2. FRAP analysis of actin turnover in whole keratocytes, Related to Figure 3. FRAP experiments are performed in whole keratocytes in the same manner as described in the main text for keratocyte fragments (Figure 3). (A) Confocal images of a live cell electroporated with two types of labeled actin, Alexa Fluor 647-actin (magenta) and Alexa Fluor 488-actin (green). (B) Kymographs showing the intensity as a function of time along a line perpendicular to the leading edge for the cell shown in (A). The bleached channel (magenta; Alexa Fluor 647-actin) and the ratio between the bleached channel and the control channel (grey; Alexa Fluor 647-actin/ Alexa Fluor 488-actin) are depicted. Scale bar: 2µm. (C) The ROI ratio intensity (Alexa Fluor 647-actin/ Alexa Fluor 488-actin) as a function of time after bleaching is measured in individual cells, and normalized by setting the pre-bleach value to 1. The average normalized ROI ratio intensity from a population of cells (N=16) is plotted as a function of time after bleaching (line) together with the standard deviation (shaded region). The average recovery is fit

to an exponential function $R(t)=(1-\varepsilon)-\alpha\cdot e^{-\frac{t}{\tau}}$ with τ,α,ε as fit parameters. (D) ROI ratio intensity profiles from individual cells are fit to an exponential as in (C). A histogram of fitted recovery times (τ) from individual cells is depicted. The average recovery time is 4.6 ± 2.6 sec (mean ± std; N=16). (E) A histogram of the fraction of diffusible actin (= 1 – ΔR) in a population of cells is shown. The average diffusible actin fraction determined from the FRAP experiments is 0.65 ± 0.15 (mean ± std; N=16). (F) FRAP analysis of actin turnover as a function of distance from the leading edge. The recovery rate (top) and fraction of diffusible actin (bottom) are determined from analysis of FRAP experiments performed in fragments (Figure 3) and whole keratocytes (A-E). The results for individual fragments (left) and whole cells (right) are plotted as a function of the distance of the bleached region from the leading edge.

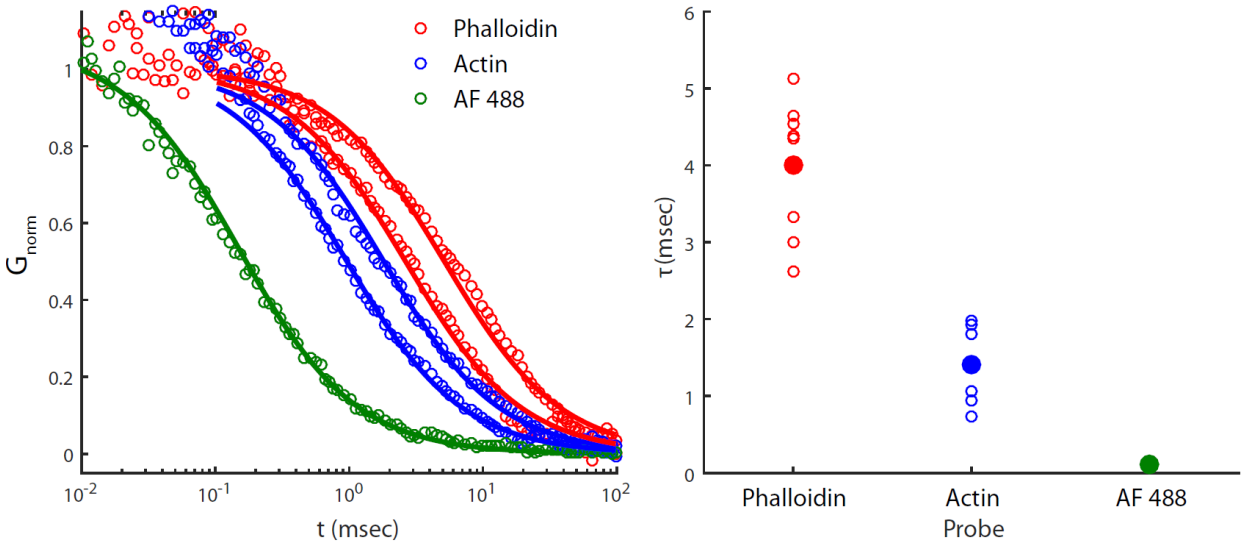

Figure S3. FCS analysis of the diffusible actin pool in individual fragments, Related to Figure 4. Left: Examples of the normalized FCS correlation as a function of lag time in individual fragments for the different probes used: Alexa Fluor 488-actin, Alexa Fluor 488-phalloidin and Alexa Fluor 488. The measured correlation functions (circles), are shown together with the best fit to a simple 2D diffusion model (lines; see Experimental Procedures). Results from two different fragments are depicted for Alexa Fluor 488-actin and Alexa Fluor 488-phalloidin to illustrate the fragment-to-fragment variability. Right: The diffusion times for individual fragments determined from fits to a simple 2D diffusion model (open circles) and their average value (filled circles) are shown for each probe.

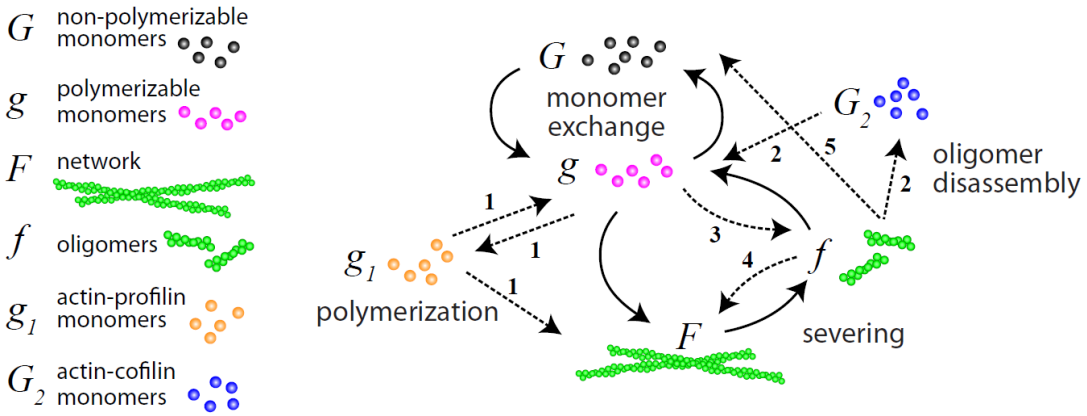

Figure S4. Alternative reaction networks for lamellipodial actin turnover, Related to Figure 5 and STAR Methods. Schematic illustrations of five possible modifications of the actin reaction network. These modifications are: (1) Addition of profilin-actin monomers which can exchange with the polymerizable monomers, and assemble into the network. (2) Addition of cofilin-actin monomers which are generated from disassembling oligomers and can dissociate from cofilin to become polymerizable monomers. (3) Allowing assembly of monomers onto the ends of oligomers. (4) Allowing assembly of oligomers into the actin network. (5) Adding oligomer disassembly into non-polymerizable actin. All these alternatives reaction networks are considered in the STAR Methods section, and shown not to affect the qualitative conclusions of the model.

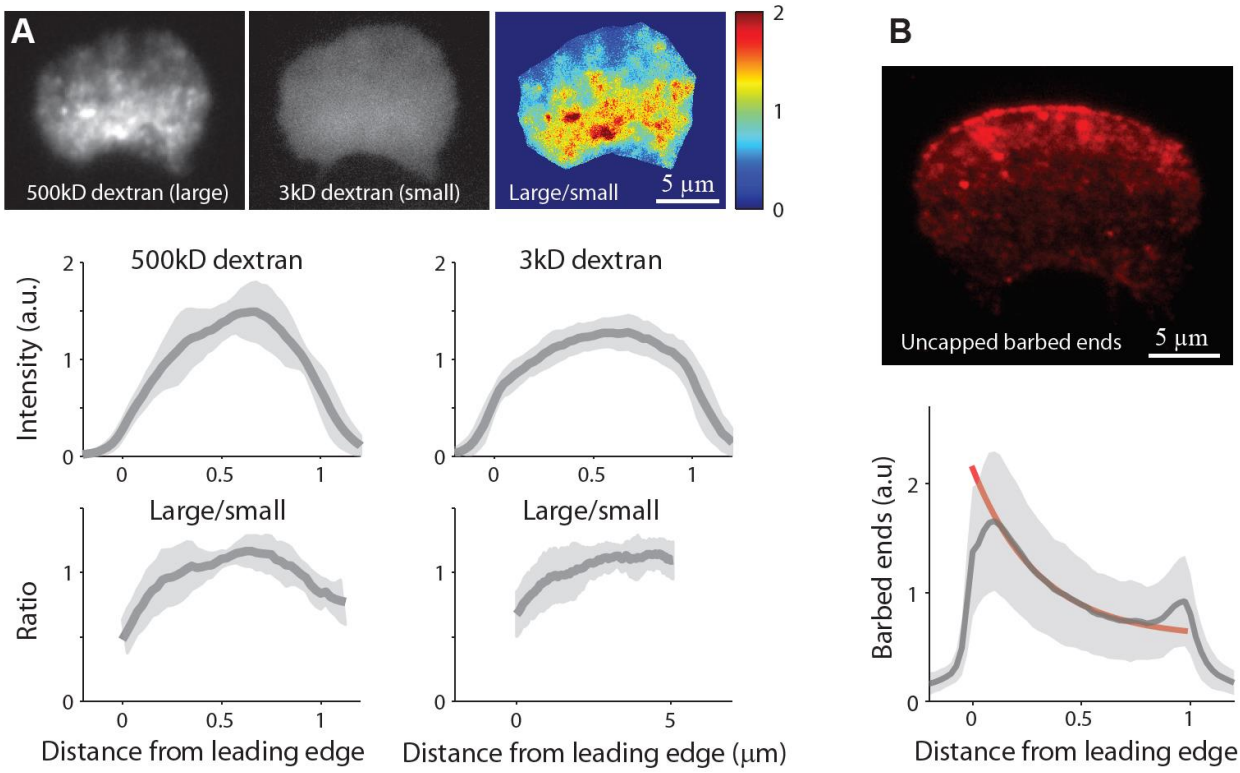

Figure S5. (A) Measurements of the intracellular fluid flow in motile fragments, Related to Figure 5 and STAR Methods. The fluid flow in motile fragments is inferred from the flow induced size-dependent distribution of probes as previously done in whole keratocytes [S1]. Top: Fluorescence images of a live fragment showing the distribution of a small probe (left; Texas red conjugated 3kD dextran), a large probe (middle; Fluorescein-conjugated 500kD dextran), and the ratio between large probe to small probe (right). The large probe density is lower near the leading edge. Bottom: Plots of the probes' density, along a cross section perpendicular to the leading edge, as a function of the normalized distance from the leading edge (top), and of the ratio density (large probe/ small probe) as a function of the normalized distance from the leading edge (bottom left) or actual distance from the leading edge (bottom right). The population-average densities (N=28; thick line) are plotted together with the standard deviation (shaded region). The large probe density is diminished near the leading edge, consistent with a fluid flow directed rearward in the frame of reference of the moving fragment. The magnitude of the flow can be estimated from the size-dependent distribution of probes which is expected to be exponential $\propto \exp\left[V_f x / D\right]$, where D is the size-dependent diffusion coefficient and V_f is the fluid velocity. The magnitude of fluid flow in fragments is similar to whole cells, but the fluid velocity is directed in the opposite direction. Specifically, the fluid flow in fragments is directed rearward, whereas in cells the flow is directed towards the leading edge. This difference is likely due to the larger concentration of myosin at the cell rear, which generates pressure and drives forward fluid flow. In both cases, as explained in the STAR Method section, the flow has a small influence on the distribution of diffusible actin monomers and oligomers. **(B) The distribution**

of uncapped barbed ends. A fluorescence image showing the distribution of uncapped barbed ends in a fragment (top) and a graph of the average intensity along a cross section perpendicular to the leading edge as a function of the normalized distance from the leading edge (bottom). The measured distribution of uncapped barbed ends (Figure 2D; grey line) is fit to a function of the form: $b(x) \approx \lambda_1 + \lambda_2 \times \exp(-x/\lambda_3)$ (red line). The best fit parameters are $\lambda_1 = 0.6$ and $\lambda_2 = 1.6$ which are non-dimensional, and $\lambda_3 = 3.3\mu m$ (x is also measured in μm). This functional form for the uncapped barbed ends distribution is used in the model.

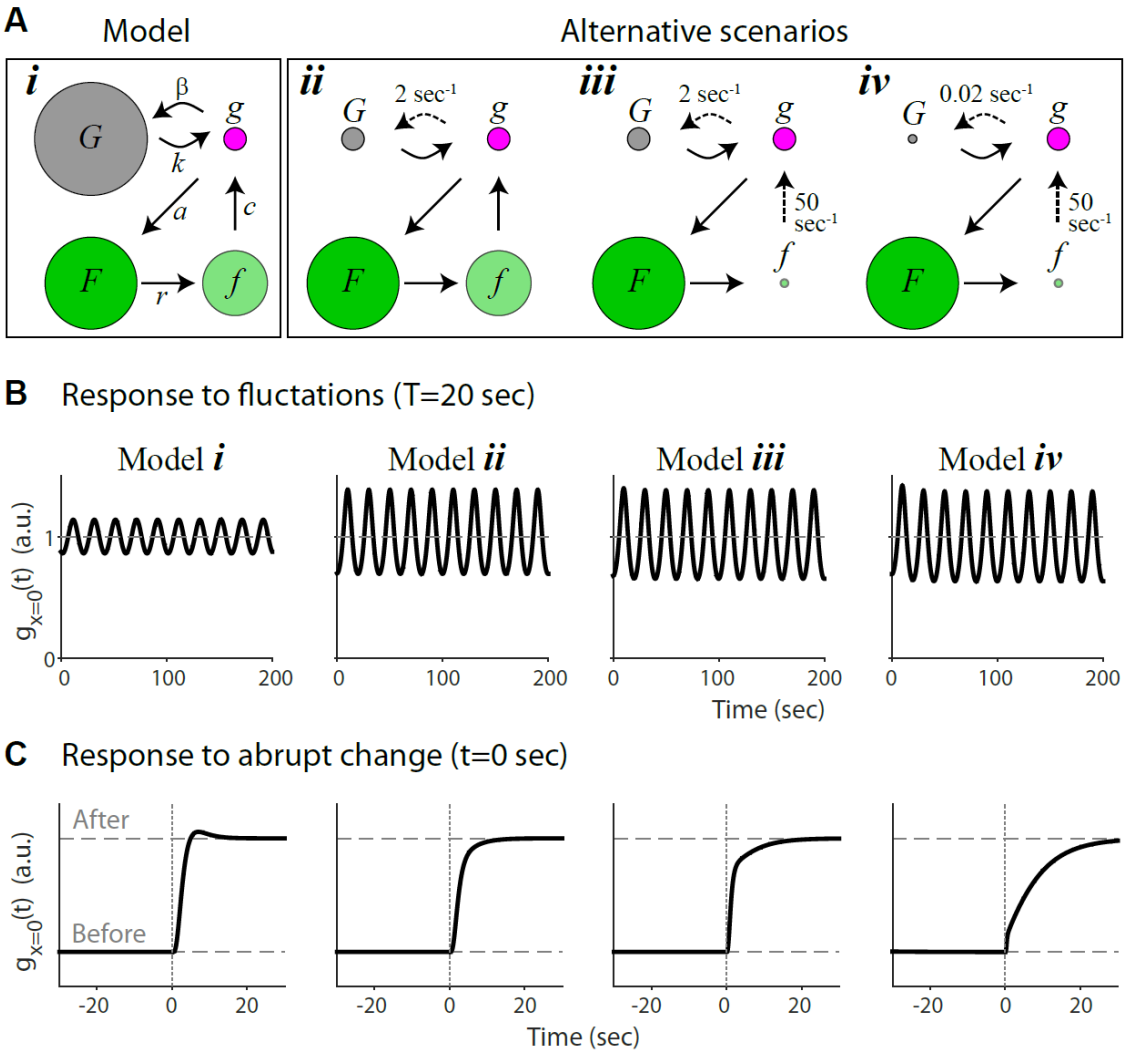

Figure S6 – Implications of the model with regards to the dynamic response of the lamellipodium to perturbations, Related to STAR Methods. (A) The general properties of lamellipodial actin turnover are highlighted by examining the system's response to changes in actin disassembly rates for four different scenarios: (*i*) the model described in the text which

includes large pools of oligomers and non-polymerizable actin monomers (G , f >> g); (*ii*) the same model as (*i*), except for taking a lower rate of monomer sequestration (β = 2/sec), so the size of the non-polymerizable actin monomer pool becomes comparable to the polymerizable actin pool ($G \approx g$, f >> g); (*iii*) same as (*ii*), adding a sharp increase in the rate of oligomer disassembly (c = 50 /sec), so the oligomer concentration becomes close to zero ($G \approx g$; $f \approx 0$); (*iv*) same as (*iii*), but imposing a further reduction in the rate of monomer sequestration (β = 0.02/sec), so the non-polymerizable actin monomer also becomes negligible ($G \approx f \approx 0$). (B) The stability of lamellipodial protrusion is probed by varying the extent of assembly at the lamellipodial front periodically by 30%, and following the concentration of polymerizable actin monomers at the leading edge, as a proxy for cell speed. The large non-polymerizable actin pool in model (*i*) buffers against fluctuations, leading to diminished (~ 15%) variation at the leading edge. In contrast, in the absence of a large non-polymerizable actin monomer pool in scenarios (*ii-iv*), large changes in the polymerizable actin monomer concentration (~ 40%) at the leading edge are apparent, and would lead to significant variations in cell speed over time. (C) The ability of the system to respond to external cues is examined by inducing a step-like, five-fold increase in the actin disassembly rate at the rear quarter of the fragment, and following the system's response over time. The concentration of polymerizable actin monomers at the leading edge is plotted as a function of time from the induced change, relative to its steady state levels before and after the perturbation (dashed lines). In both models (*i*) and (*ii*), the concentration of polymerizable actin at the leading edge increases to approximately its new steady state value within ~ 3 seconds. The response time of the system is an order of magnitude longer in scenarios (*iii*) and (*iv*). In scenario (*iv*), in the absence of both diffusing oligomers and a large, rapidly exchanging, pool of non-polymerizable actin, it takes ~20 sec for the polymerizable actin concentration at the leading edge to increase substantially.

Supplemental Reference

S1. Keren K, Yam PT, Kinkhabwala A, Mogilner A, Theriot JA (2009) Intracellular fluid flow in rapidly moving cells. Nat Cell Biol 11: 1219-1224